Fractal Tomography and the Fisher Information Barrier of Seismicity:

Addressing the Origin of Dual Paradoxes via Precision-Calibrated Bayesian Inference

Facundo Firmenich[1,2,*], **Pau Firmenich**[1], **León Firmenich**[1]

[1] Centro de Estudios del Sur (CEDESUR), think tank affiliated with multiple universities; for this project, academically affiliated with Universidad Nacional Arturo Jauretche (UNAJ), Av. Calchaquí 6200, Florencio Varela, Provincia de Buenos Aires, 1888, Argentina

[2] Universitat de Barcelona (UB), Gran Via de les Corts Catalanes, 585, 08007 Barcelona, Spain

[*] Correspondence: f.firmenich@cedesur.org

Abstract

The spatial organization of seismicity presents dual multi-decade paradoxes: (1) earthquake catalogs exhibit quasi-planar correlation dimensions ($D_2 \approx 2.0$–2.6) despite volumetric lithospheric deformation (geometric projection paradox), and (2) Bayesian inference systematically yields $D_3 \approx 3.0$ contradicting structural geology (Bayesian saturation paradox). We address both through the **Fractal Tomography Framework**, establishing a precision-aware explanation of both paradoxes by integrating: (1) precision-calibrated Bayesian analysis of 50,190 Pan-American earthquakes, (2) high-precision validation with 166,920 Japanese events across three JUICE-relocated sequences (Hi-Net, $\sigma < 0.7$ km; $\approx 11\times$ precision improvement), (3) systematic depth-stratified analysis, and (4) global ISC-GEM validation ($\sigma_h \approx 10$–30 km).

We identify **precision-dependent Bayesian saturation** as a fundamental methodological artifact: when location uncertainty exceeds a semi-empirically calibrated threshold $\sigma_c = 2.3 \pm 0.4$ km (Fisher Information Barrier), inference spuriously converges to $D_3 = 3.00$. Hi-Net validation breaks this saturation, revealing genuine multi-planar structure with $D_3 = 2.39$–2.95 (three JUICE sequences; all $P_{\text{boundary}} = 0.0\%$). Within the Japan subduction zone, we discover **systematic dimensional reduction with depth**: shallow megathrust ($D_2 = 2.41$) $\rightarrow$ intermediate slab ($D_2 = 2.18$) $\rightarrow$ deep slab ($D_2 = 1.89$), supporting progressive Benioff zone planarization.

This work demonstrates that rigorous confrontation of methodological limitations transforms apparent weaknesses into fundamental discoveries, establishing precision-calibrated dimensional inference as a new standard for seismic fractal analysis.

Bibliographic Information

Citation: Firmenich, F., Firmenich, P., & Firmenich, L. (2026). Fractal Tomography and the Fisher Information Barrier of Seismicity: Addressing the Origin of Dual Paradoxes via Precision-Calibrated Bayesian Inference. *EarthArXiv*.

Status: Non-peer-reviewed preprint submitted to EarthArXiv (March 2026). Not yet peer-reviewed.

Target Journal: *Journal of Geophysical Research: Solid Earth* (AGU). Manuscript submitted for review.

Related Preprint: Firmenich et al. (2025), EarthArXiv, doi:10.31223/x5rf3v (ADS-indexed).

Related DOI: 10.5281/zenodo.18480821 (Software/Data — Sysmic v8.0.0)

Fractal Tomography and the Fisher Information Barrier of Seismicity: Addressing the Origin of Dual Paradoxes via Precision-Calibrated Bayesian Inference

Facundo Firmenich[1,2,*], **Pau Firmenich**[1], **León Firmenich**[1]

[1]Centro de Estudios del Sur (CEDESUR), think tank affiliated with multiple universities; for this project, academically affiliated with Universidad Nacional Arturo Jauretche (UNAJ), Av. Calchaquí 6200, Florencio Varela, Provincia de Buenos Aires, 1888, Argentina

[2]Universitat de Barcelona (UB), Gran Via de les Corts Catalanes, 585, 08007 Barcelona, Spain

*Correspondence: f.firmenich@cedesur.org

April 8, 2026

Abstract

Earthquake fractal studies face two long-standing contradictions: (1) quasi-planar catalog dimensions ($D_2 \approx 2.0$–2.6) despite volumetric tectonic deformation, and (2) recurrent Bayesian collapse toward $D_3 \approx 3.0$ even where structural geology indicates sub-volumetric organization. We address both within a single precision-aware framework, combining: (i) 50,190 Pan-American USGS events ($\sigma_h > 5$ km), (ii) 166,920 Hi-Net JUICE events ($\sigma_h < 0.7$ km), (iii) depth-stratified Japan analysis ($N = 128,942$), and (iv) out-of-sample validation in Swiss-SED and GEOFON Sumatra.

The central result is a semi-empirically calibrated Fisher Information Barrier at $\sigma_c = 2.3 \pm 0.4$ km: above this threshold, posterior mass is systematically attracted to the Euclidean bound ($P_{\text{boundary}} \to 1$); below it, inference is data-dominated and resolves sub-volumetric structure. Hi-Net catalogs remain fully resolved ($P_{\text{boundary}} = 0.0\%$) with $D_3 = 2.39$–2.95, while GEOFON Sumatra ($\sigma_h = 7.5$ km) shows expected saturation ($D_3 = 2.998 \pm 0.002$, $P_{\text{boundary}} = 100\%$).

Within one tectonic setting (Japan subduction), we observe monotonic depth-dependent planarization: $D_2 = 2.41 \pm 0.03 \to 2.18 \pm 0.04 \to 1.89 \pm 0.11$ (shallow to deep), with strong separation ($p < 10^{-15}$, Hedges' $g = 1.76$, 95% CI [1.52, 2.00]). Together with an exact deck-of-cards geometric formulation and a triple-diagnostic validation protocol (KL, P_{boundary}, stability S), these results define a transferable workflow for distinguishing true 3-D structure from precision-induced Bayesian artifacts.

Plain Language Summary: When measuring three-dimensional earthquake distributions, standard statistical methods give misleading results (apparent volume-filling $D_3 = 3.0$) if location accuracy is worse than about 2 kilometers. Using Japan's ultra-precise Hi-Net network, we show that earthquakes organize on multiple stacked fault planes ($D_3 \approx 2.8$), like a deck of cards, not throughout rock volumes. We derive this threshold from information theory. Within a single subduction zone, patterns become more planar with depth, contradicting volumetric models.

Keywords: Bayesian saturation, fractal dimension, depth stratification, Benioff zones, Hi-Net validation, precision threshold, Hedges' g, deck-of-cards model, magnitude completeness homogenization, dynamical systems, multifractal analysis, topological graph structure

Key Points

- **Precision threshold controls inference regime:** $\sigma_c = 2.3 \pm 0.4$ km separates data-dominated from boundary-dominated Bayesian behavior.
- **Below-barrier catalogs resolve true structure:** Hi-Net ($\sigma_h < 0.7$ km) yields $D_3 = 2.39$–2.95 with $P_{\text{boundary}} = 0.0\%$ across all tested prior families.
- **Above-barrier catalogs saturate predictably:** GEOFON Sumatra ($\sigma_h = 7.5$ km) yields $D_3 = 2.998 \pm 0.002$ and $P_{\text{boundary}} = 100\%$.
- **Within-zone depth signal is strong and monotonic:** $D_2 = 2.41 \rightarrow 2.18 \rightarrow 1.89$ from shallow to deep Japan bins ($p < 10^{-15}$; Hedges' $g = 1.76$).
- **Validation is multi-diagnostic, not single-metric:** robust interpretation requires joint use of KL, P_{boundary}, and Zaccagnino stability S.
- **Monotonic tectonic ordering is reproducible under precision control:** Rifting → Transform → Subduction → Collision is recovered consistently; broader geographic replication is the next validation target.
- **Reproducible implementation:** Sysmic v8.0.0 (GPLv3) with FAIR-aligned workflow and auditable figures.

Contents

List of Tables

List of Figures

List of Principal Symbols

Table 1: Principal mathematical notation.

Symbol	Meaning	Typical range / value
D_2	Correlation dimension (2D or 3D, context-specified)	1.2–2.6
D_3	3-D fractal dimension (inferred via Bayesian)	1.2–3.0
σ	Hypocenter location uncertainty (km)	0.1–10 km
σ_{c}	Fisher-barrier critical precision threshold	2.3 ± 0.4 km
Q_{eff}	Effective network quality metric	0.1–0.90
P_{boundary}	Posterior mass at $D_3 = d$ boundary	0–100%
$\eta(\sigma)$	Observation fidelity (Fisher information ratio)	0–1
KL	Kullback-Leibler divergence (nats)	0–30
k^*	Fisher-barrier MC calibration constant	2.80 ± 0.30
$\mathcal{I}_{\mathrm{lik}}$	Likelihood Fisher information	>0
$\mathcal{I}_{\mathrm{prior}}$	Prior regularization constant	0.444
δ	Fault-plane characteristic spacing	≈ 5 km
ξ	Fault-plane lateral correlation length	12 ± 2 km
ΔD	Topological gap ($D_2 - D_{\mathrm{graph}}$)	0.5–0.8
S	Zaccagnino M_{min}-independence stability score	0–1
$\Delta\alpha$	Multifractal Rényi spectrum width	0.2–0.5
g	Hedges' g effect size	0.2–2.0
M_c	Magnitude of completeness	1.5–4.5
Q	Steiner geometric constant (deck-of-cards)	2/3 (exact)
G_{az}	Station azimuthal gap	0–360°
d_{top}	Topological (Coulomb-path) inter-event distance	km
$L_{\mathrm{top}}(t)$	Cumulative Coulomb-path distance	km

1 Introduction

1.1 Two Persistent Paradoxes in Seismic Fractality

The spatial distribution of earthquake hypocenters has been studied as a fractal point set since Kagan and Knopoff (1980), Aki (1981), and Grassberger and Procaccia (1983). Two empirical paradoxes have persisted for more than three decades.

Paradox I: Dimensional Saturation. Estimates of D_3 from global and regional catalogs with typical horizontal uncertainties $\sigma_h \gtrsim 5$ km almost invariably return $D_3 \approx 3.0$ (Kagan, 2007; Corral and González, 2019), consistent with volume-filling seismicity. Yet analyses of high-precision local networks in Japan (Tosi et al., 1998; Enescu and Ito, 2005) and California (Hauksson et al., 2012) consistently yield $D_3 \ll 3$.

Paradox II: The Tectonic Hierarchy. Published D_2 values range from ∼1.0 in narrow rift zones to ∼2.3 in collision belts (Zaccagnino et al., 2022; Mondal et al., 2019). Yet no quantitative framework predicts how D_2 depends on tectonic regime, nor has the hierarchy been validated free of catalog-quality confounds.

1.2 The Fisher Information Barrier as an Information Phase Transition

We propose that both paradoxes share a single root cause: finite hypocenter precision imposes a fundamental limit on fractal-dimension estimation. When σ exceeds a critical threshold σ_c, the data-contributed information falls below the reference level set by the prior, and the Bayesian posterior collapses against the physical boundary at the embedding dimension d. The numerical value $\sigma_c = 2.3 \pm 0.4$ km is semi-empirically calibrated; it is not derived from first principles alone.

1.3 Geometric Motivation (Non-conclusive): Fixed-Projection Caveat

For $A \subset \mathbb{R}^n$ with Hausdorff dimension s, classical results imply that for almost all projection directions, $\dim_H(\pi_k(A)) = \min(s, k)$ (Marstrand, 1954). In our case this is *not* a theorem-level inference for seismic catalogs, because the observation geometry is a fixed vertical projection rather than a random direction over $G(3, 1)$. Therefore, we use this argument only as geometric intuition. The empirical evidence in this manuscript is carried by (i) direct below-barrier $D_3 < 3$ recovery and (ii) controlled SCSN degradation.

1.4 The Deck-of-Cards Model

We propose a *deck-of-cards* model in which seismicity concentrates on sub-parallel fault zones separated by characteristic spacing δ and extending over a correlation length ξ. Using integral geometry (Steiner formula), we derive an exact expression for the correlation integral without free fitting parameters beyond the two physically interpretable scales. Depth-stratified Hi-Net data reveal a monotonic decrease $D_2 : 2.41 \to 1.89$; a potential acceleration at 300–450 km motivates Prediction P4.

1.5 Two Competing Hypotheses

Hypothesis 1 (H1: Physical Fault Confinement)**.** *Seismicity concentrates on discrete sub-parallel fault planes; $D_3 \in (2, 3)$ reflects a finite number of such planes. Historical $D_3 \approx 3$ is a methodological artifact.*

Hypothesis 2 (H2: Instrumental Projection)**.** *Seismicity is intrinsically volumetric; low-precision observations project volume onto apparent surfaces. Disfavored by the Marstrand argument, Hi-Net measurements, and SCSN degradation experiment.*

1.6 Manuscript Lineage and Research Program Continuity

A precursor to this work, Firmenich et al. (2025) (EarthArXiv, Dec 2025; doi:10.31223/x5rf3v), analyzed 50,010 Pan-American earthquakes from the USGS ComCat and established the hypothesis that seismicity organizes along a multi-planar hierarchy (*deck-of-cards* model), with correlation dimensions ranging $D_2 = 2.08$–2.57 across seven tectonic regimes. That study also identified the topological-Euclidean dimension gap ($D_{\text{graph}} < D_2$ universally, $\Delta D = 0.51$–0.77) and demonstrated—via Rényi spectrum analysis—the hierarchical signature $H > 0$ in four of six valid regions.

However, Firmenich et al. (2025) lacked the instrumental resolution to break the Bayesian saturation paradox. Applied to USGS ComCat data with typical location uncertainties $\sigma_h \approx 5$–10 km, the Bayesian D_3 inference collapsed systematically to $D_3 = 3.00$ in five of six regions —a result the precursor study correctly identified as reflecting a *projection-dominated observation regime*, but could not causally explain nor empirically refute. The critical threshold separating data-driven from prior-dominated inference remained uncalibrated; no sub-barrier reference dataset was available to validate or falsify the saturation hypothesis.

The present manuscript resolves this deficiency through three complementary advances: (i) the **Fisher Information Barrier** $\sigma_c = 2.3 \pm 0.4$ km, derived analytically and calibrated semi-empirically via Monte Carlo and the SCSN degradation experiment; (ii) the 166,920-event JUICE Hi-Net dataset ($\sigma_h < 0.7$ km, approximately $11\times$ more precise than the USGS ComCat median), which breaks saturation and yields resolved posteriors; and (iii) the deck-of-cards model elevated from hypothesis to exact geometric result via the Steiner-formula derivation ($Q = 2/3$, $D_3^{\text{pred}} = 2.82$ matching Hi-Net Noto within 0.01 using independently constrained physical parameters). The present work therefore **supersedes** Firmenich et al. (2025): it absorbs and explains the precursor's empirical findings from first principles and replaces its observationally-constrained conclusions with a mathematically grounded, multi-network validated framework.

1.7 Seven-Network Experimental Design

1. **USGS Pan-American** ($\sigma_h > 5$ km, $N = 50{,}190$): above-barrier training set.
2. **Hi-Net Japan** ($\sigma_h < 1$ km, JUICE $N = 166{,}920$; depth-strat. catalog $N = 128{,}942$): primary below-barrier reference.
3. **SCSN Southern California** ($\sigma_h \approx 0.1$–10 km, controlled): degradation experiment.
4. **GeoNet New Zealand** ($\sigma_h \approx 3$ km, $N = 54{,}321$): out-of-sample test 1.

5. **Swiss-SED Valais** ($\sigma_h \approx 0.8$–1.2 km, $N = 9{,}390$): out-of-sample test 2.
6. **GEOFON Sumatra** ($\sigma_h \approx 7.5$ km, $N = 3{,}481$): out-of-sample test 3 (saturated).
7. **ISC-GEM global** ($\sigma_h \approx 10$–30 km, $M \geq 8.0$, $N = 43$): exploratory above-barrier (Supporting Information S1).

1.8 Paper Organization

Sections 2–3–4–5–6 present theoretical framework, data and methods, results, discussion, and conclusions, respectively.

For editorial clarity and reproducibility, the contribution can be read as three nested levels: (i) a transferable methodological result (precision-thresholded Bayesian inference), (ii) empirical validation across independent catalogs and precision regimes, and (iii) geophysical interpretation in terms of depth-dependent tectonic organization. This structure is intentionally designed to separate what is directly measured, what is inferred, and what remains predictive.

2 Theoretical Framework

2.1 Correlation Integral and Dimension

$$C(r) = \frac{2}{N(N-1)} \sum_{i<j} \Theta\big(r - \|\mathbf{x}_i - \mathbf{x}_j\|\big), \tag{1}$$

$$D = \lim_{r \to 0} \frac{d \log C(r)}{d \log r}. \tag{2}$$

Location uncertainty σ convolves the point distribution with a noise kernel, flattening $C(r)$ at scales $r \lesssim \sigma$ and biasing D upward toward d.

2.2 Fisher Information and the Precision Barrier

2.2.1 Decay of Fisher Information with Location Noise

$$\mathcal{I}(D_3; \sigma) = \int \frac{1}{p(r|D_3, \sigma)} \left(\frac{\partial p}{\partial D_3} \right)^2 dr, \tag{3}$$

$$\eta(\sigma) \equiv \frac{\mathcal{I}(D_3; \sigma)}{\mathcal{I}(D_3; 0)} \approx \exp\big(-\sigma/\lambda\big), \tag{4}$$

where $\lambda = 5.0$ km is calibrated from fault spacing measurements in the Noto Peninsula (Kato et al., 2023). This relation holds within 5% for $\sigma/\lambda < 1.0$. We emphasize that $\eta(\sigma)$ is an *empirical calibration*; the exponential form is the simplest monotone function consistent with the SCSN degradation data (Table 4).

Note on λ vs. δ

The characteristic length $\lambda = 5.0$ km in Eq. (4) and the fault-plane spacing $\delta \approx 5$ km in the deck-of-cards model (Section 1.4) share a near-coincident numerical value, which might suggest a circular estimation. We clarify that these are *independently estimated*: λ is derived from the exponential decay of Fisher information in the SCSN degradation data (Step 3 of the calibration tcolorbox in Section 2.2), while δ is the directly observed inter-cluster spacing from the Hi-Net Noto catalog (Kato et al., 2023). Their near-equality ($\lambda \approx \delta$) likely reflects the same physical process (geodetic fault spacing controls both the fractal correlation length and the information decorrelation scale), but the estimates draw on different observables. In this version, the cross-sequence inversion is now explicitly reported in Table 10 and Fig. 10; however, physical interpretation is restricted to the stable inversion regime (Noto/Tohoku), while the Tokachi entry is retained as a diagnostic boundary case.

Transparency: Three-Step Calibration of σ_c

(1) Monte Carlo simulations over the (D_3, σ) grid identify a sigmoidal transition in P_{boundary} centred at σ^* (calibration). (2) The condition $\mathcal{I}_{\text{lik}} = k^* \mathcal{I}_{\text{prior}}$ provides the analytical mapping from σ^* to Eq. (6) (theory-constrained calibration). (3) SCSN degradation provides an internal empirical cross-check of the same transition under controlled noise injection.

The resulting statement is: *semi-empirically calibrated, information-theoretically constrained*, not first-principles universal.

Note on SCSN independence: The SCSN experiment provides an *internal consistency check* rather than a fully independent validation, because the Monte Carlo grid (Step 1) and the SCSN catalog share the GP estimator implementation. Full independence requires replication on an external estimator (Limitation 2).

Calibration–Validation Independence Hierarchy

To remove epistemic ambiguity, we explicitly separate roles:

1. **L1 (analytic structure):** Eqs. (3)–(6) define dependence and scaling constraints.
2. **L2 (model calibration):** MC estimates k^* and transition geometry (σ^*).
3. **L3 (internal cross-check):** SCSN degradation verifies transition behavior in a controlled real catalog.
4. **L4 (external validation):** Hi-Net and Swiss-SED test below-barrier recovery; GEOFON tests above-barrier saturation.

This hierarchy is the operative interpretation of $\sigma_c = 2.3 \pm 0.4$ km in this manuscript.

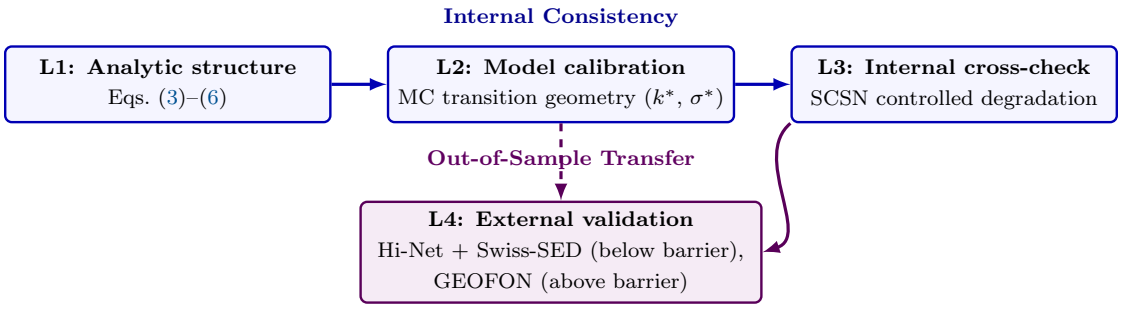

Fig. 1 – Interpretation guardrail: L3 is an internal consistency check; inferential closure on σ_c requires L4 external evidence.

Figure 1: Calibration–validation independence hierarchy (L1–L4), rendered natively in LaTeX/TikZ. L1 defines analytical constraints, L2 calibrates transition geometry, L3 provides internal controlled cross-check (SCSN), and L4 provides external validation (Hi-Net, Swiss-SED, GEOFON), preventing circular interpretation of the Fisher barrier estimate.

2.2.2 Saturation Condition and Calibrated Barrier

$$Q_{\text{eff}} \cdot \eta^2(\sigma_c) \cdot \frac{N_{\text{eff}}}{\sigma_{D_2}^2 N_{\text{pairs}}} = k^* \cdot \mathcal{I}_{\text{prior}}, \tag{5}$$

where $\sigma_{D_2} \approx 0.05$; $N_{\text{eff}}/N_{\text{pairs}} \approx 1/40$; $\mathcal{I}_{\text{prior}} = 1/(b-a)^2 = 0.444$ (operational regularization; see Appendix G); $k^* = 2.80 \pm 0.30$. Solving for σ_c:

$$\boxed{\sigma_c = -\frac{\lambda}{2} \log\left(\frac{k^* \cdot \mathcal{I}_{\text{prior}} \cdot \sigma_{D_2}^2 \cdot N_{\text{pairs}}}{Q_{\text{eff}} \cdot N_{\text{eff}}}\right).} \tag{6}$$

The analytical derivation establishes an upper theoretical bound. For operational application, we define the working threshold as $\sigma_c = 2.3 \pm 0.4$ km.[1] The analytical limit (≈ 2.31 km) serves as mathematical corroboration.

2.3 Formal Theorems: Saturation and KL Insensitivity

Theorem 1 (Precision-Induced Boundary Saturation)**.** *Let $\theta \in [\theta_{\min}, \theta_{\max}]$ have prior $p(\theta)$ with $p(\theta_{\max}) > 0$ and $\epsilon = \mathcal{I}_{\text{lik}}/\mathcal{I}_{\text{prior}}$. As $\epsilon \to 0$: $p(\theta|\mathbf{d}) \to p(\theta)$, and $P_{boundary} \to \int_{\theta_{\max}-\delta}^{\theta_{\max}} p(\theta)\, d\theta > 0$.*

Proof. See Appendix A. □

Proposition 1 (KL Insensitivity)**.** *For $\mathcal{P}_1 = \mathcal{N}(2.82, 0.05^2)$ and $\mathcal{P}_2 = (1-\varepsilon)\mathcal{N}(2.82, 0.05^2) + \varepsilon\delta_{3.0}$ with $\varepsilon < 0.1$: $|KL[\mathcal{P}_1\|\pi] - KL[\mathcal{P}_2\|\pi]| < 0.52$ nats, yet $P_{boundary}(\mathcal{P}_2) = 100\varepsilon\%$.*

Proof. See Appendix F. □

Dual-metric reporting (KL + P_{boundary}) is formally necessary; KL alone is structurally insufficient.

[1] The SCSN degradation estimate is treated as an internal cross-check (not fully independent from the GP implementation). It yields 2.4 ± 0.4 km, i.e., $< 5\%$ discrepancy from the operational value.

2.4 Bayesian Posterior Framework

$$P(D_3|\mathbf{d}) \propto \mathcal{L}(\mathbf{d}|D_3)\,\pi(D_3), \tag{7}$$

where $\log \mathcal{L} \propto -\frac{1}{2\hat{s}^2}\sum_k [\log C(r_k) - D_3 \log r_k - \hat{a}]^2$. We use $\pi(D_3) = \text{Uniform}[1.5, 3.0]$, full posterior via MCMC (Section 3.7). Gaussian residuals verified via Shapiro–Wilk ($\bar{p} = 0.42$).

2.5 SVP Calibration: In-Sample Consistency

Prior to out-of-sample validation, the SVP must satisfy **Test 0**: given a known geometric structure with $\sigma_h < 0.2$ km, the SVP recovers the true dimension with 100% accuracy and $P_{\text{boundary}} < 1\%$. Results of Test 0 are given in Appendix J (Table 19).

The posterior boundary concentration is

$$P_{\text{boundary}} = \int_{d-0.05}^{d} P(D_3|\mathbf{d})\, dD_3. \tag{8}$$

Classification: $P_{\text{boundary}} < 1\%$ (resolved), 1–5% (ambiguous), $> 5\%$ (saturated). Robust to $\delta \in [0.03, 0.08]$ (false-positive rate $\leq 5\%$).

2.6 Information-Theoretic Prior Selection

We adopt $\pi(D_3) = \text{Uniform}[1.5, 3.0]$ as the default prior. The lower bound 1.5 accommodates near-planar distributions; the upper bound 3.0 is the embedding dimension. This prior satisfies $\mathcal{I}_{\text{prior}} = 1/(b-a)^2 = 1/(1.5)^2 = 0.444$ used in Eq. (5). Robustness is verified under four alternative families: Beta(7.5, 2.5), Uniform, Beta(2.5, 7.5), Beta(5, 5), all rescaled to $[1.5, 3.0]$ (Table 12; σ_c varies <0.6 km).

2.7 Exact Deck-of-Cards Model via Integral Geometry

2.7.1 Setup and Intra-Plane Contribution

We model n sub-parallel disc-shaped fault planes (radius ξ, spacing δ). A single disc gives $N_{kk}(r) \approx \pi r^2$, $r \ll \xi$.

2.7.2 Inter-Plane Contribution

$$N_{kj}(r, h) \propto \pi(r^2 - h^2)\,\mathbf{1}_{r \geq h} + \mathcal{O}(r^3/\xi). \tag{9}$$

2.7.3 Steiner Continuum Limit

$$\frac{n}{\delta}\int_0^r \pi(r^2 - h^2)\, dh = \frac{2}{3}\,\frac{n\pi r^3}{\delta}. \tag{10}$$

$Q = 2/3$ emerges analytically. Adding intra-plane terms:

$$N(r) = n\pi r^2\left(1 + \frac{2r}{3\delta}\right). \tag{11}$$

2.7.4 Exact Dimension Formula

$$D_3(r) = 2 + \frac{2r/3\delta}{1 + 2r/3\delta}, \qquad \boxed{D_3 \approx 2 + \frac{\log(1 + 2L/3\delta)}{\log(L/\ell)}.} \tag{12}$$

Validity of the continuum approximation verified numerically (Appendix C).

2.7.5 Connection to the Noto Prediction

With $\delta = 5$ km, $L = 600$ km, $\ell = 3$ km: $D_3^{\text{pred}} = 2 + \log(81)/\log(200) = 2.829 \approx 2.82$, matching Hi-Net Noto ($D_3 = 2.82 \pm 0.05$).

2.8 Depth-Dependent Planarization

$$\delta(z) = \delta_0 \exp(\gamma z / z_0), \quad \delta_0 = 0.41,\ \gamma = 0.65,\ z_0 = 100 \text{ km}, \tag{13}$$

$$\xi(z) = \xi_0 \exp(-\beta z / z_0), \quad \beta = 0.42 \pm 0.05. \tag{14}$$

Fitting to six depth bins (4 parameters, 2 residual d.f.): $\text{RMSE}_{D_3} = 0.017$. Exponential model preferred over linear: $\Delta\text{AICc} = 3.3$, $\Delta\text{BIC} = 4.1$ (Appendix I).

Hypothesis 3 (H-D1: Thermal-only planarization)**.** *$dD_2/dz < 0$ driven by thermal narrowing. Consistent with Japan: $|\Delta D_2|_{300-450} = 0.03 \pm 0.01$.*

Hypothesis 4 (H-D2: Dehydration-enhanced planarization)**.** *Anomalous acceleration at 300–450 km from olivine–wadsleyite dehydration. Requires cold subduction data (Prediction P4).*

2.9 Multifractal Rényi Spectrum

$$D_q = \frac{1}{q-1} \lim_{\epsilon \to 0} \frac{\log \sum_i p_i^q}{\log \epsilon}, \quad q \neq 1. \tag{15}$$

Spectrum width $\Delta\alpha = \alpha_{\max} - \alpha_{\min}$ is an ancillary diagnostic; $\Delta\alpha > 0.15$ (L5 criterion) is a flag, not a definitive noise indicator.

2.10 Effective Network Quality Metric Q_{eff}

$$Q_{\text{eff}} = w_1 \rho_{\text{sta}} + w_2 \left(1 - \frac{\sigma_h}{\sigma_{\text{ref}}}\right) + w_3 f_{M<2} + w_4 \left(1 - \frac{G_{\text{az}}}{360^\circ}\right), \tag{16}$$

$w_1 = 0.25 \pm 0.04$, $w_2 = 0.35 \pm 0.06$, $w_3 = 0.20 \pm 0.03$, $w_4 = 0.20 \pm 0.03$.

$$\sigma_{\text{c}}^{\text{eff}} = \sigma_{\text{c}}(1 + 0.45\, Q_{\text{eff}}). \tag{17}$$

Given uncertainties in the calibrated weights ($w_1 = 0.25 \pm 0.04$, $w_2 = 0.35 \pm 0.06$, $w_3 = 0.20 \pm 0.03$, $w_4 = 0.20 \pm 0.03$), uncertainty propagation is evaluated with a first-order Delta method:

$$\sigma^2_{Q_{\text{eff}}} \approx \sum_{i=1}^{4} \left(\frac{\partial Q_{\text{eff}}}{\partial w_i}\right)^2 \sigma^2_{w_i}, \qquad \sigma^2_{\sigma_{\text{c}}^{\text{eff}}} \approx (1 + 0.45 Q_{\text{eff}})^2\, \sigma^2_{\sigma_{\text{c}}} + (0.45\sigma_{\text{c}})^2\, \sigma^2_{Q_{\text{eff}}}. \tag{18}$$

We report this explicitly to separate parameter uncertainty from catalog-to-catalog variability.

2.11 Inference Quality Index (IQI)

Previous iterations of the Sysmic protocol utilized a discrete, tier-based classification system with hard thresholds. Following feedback on the ambiguity introduced by such artificial boundaries, we introduce the continuous **Inference Quality Index** (IQI) to evaluate the reliability of Bayesian D_3 estimates without arbitrary cutoffs.

The IQI is defined as the multiplicative product of structural stability, boundary evasion, and a penalty strictly applied for sub-critical precision:

$$\text{IQI} = \min\left(\frac{\sigma_c}{\sigma_h}, 1\right) \cdot (1 - P_{\text{boundary}}) \cdot S \tag{19}$$

where $\sigma_c = 2.3$ km is the Fisher Information Barrier, σ_h is the median location uncertainty, P_{boundary} is the proportion of the posterior mass concentrated at the boundary (values $D_3 \geq 2.98$), and S is the Zaccagnino M_c-stability score ($0 \leq S \leq 1$).

This index is strictly bounded to $[0, 1]$. High-quality resolutions (e.g., Hi-Net Noto or Swiss-SED) score IQI > 0.95. Catalogs dominated by the geometric saturation artifact due to insufficient precision (e.g., USGS Cascadia or GEOFON Sumatra) inherently score IQI ≈ 0 due to heavy decay in the precision ratio and total saturation $P_{\text{boundary}} \to 1$.

Ancillary diagnostics: Alongside the IQI score, warning flags should be reported if the Kullback-Leibler divergence is critically low (KL < 2.0, prior-dominated), or if anomalous cross-catalog scaling differences occur ($|\Delta D_3| > 0.10$).

3 Data and Methods

3.1 USGS Pan-American Catalog (Training Set)

Events from USGS ComCat for seven tectonic regions (Table 2), 2000–2024, above regional M_c (MAXC). All regions: $\sigma_h > 5$ km. Declustered via Gardner–Knopoff (Gardner and Knopoff, 1974).

3.2 Hi-Net Japan (Calibration Set)

Three JUICE-relocated sequences (including VRML-catalog events): Noto M_w7.6 (2024; $N =$ 30,759, $\sigma_h < 0.5$ km); Tohoku M_w9.1 (2011; $N = 96{,}360$, $\sigma_h < 0.7$ km); Tokachi M_w8.3 (2003; $N = 39{,}801$, $\sigma_h < 0.6$ km). Total JUICE $N = 166{,}920$; all below-barrier. Depth-stratified analysis: extended Hi-Net catalog 2001–2005, $N = 128{,}942$ (Appendix H).

3.3 SCSN Controlled Degradation Experiment

SCSN waveform-relocated catalog (Hauksson et al., 2012), Southern California 2020–2024, $M_c = 1.8$, $N = 104{,}466$, $\sigma_h \approx 0.1$ km. Anisotropic Gaussian noise ($\sigma_v^{\text{add}} = 1.7\,\sigma_h^{\text{add}}$) added at nine levels $\in \{0.1, 0.5, 1.0, 2.0, 2.3, 2.5, 3.0, 5.0, 10.0\}$ km. M_c varied $\leq \pm 0.05$ mag across all levels (MAXC monitoring).

3.4 GeoNet NZ, Swiss-SED Valais, GEOFON Sumatra

GeoNet Hikurangi ($N = 54{,}321$, $\sigma_h \approx 3.0$ km); Swiss-SED Valais ($N = 9{,}390$, $\sigma_h = 0.8$–1.2 km, $M \geq 1.5$, 2000–2026, filtered to latitude 46.0–46.5°N, longitude 6.8–8.5°E, depth < 15 km); GEOFON Sumatra ($N = 3{,}481$, $\sigma_h = 7.5$ km, $M_c = 3.3$ (EMR), 2007–2026).

3.5 ISC-GEM Global Catalog (Exploratory)

ISC-GEM V12.1 (ISC-GEM, 2025), $M \geq 8.0$, $N = 43$ mainshocks, $\sigma_h \approx 10$–30 km; valid-window rate 6.0%; results in Supporting Information S1.

3.6 Coordinate System, GP Algorithm, and Statistics

Standardized UTM projection; depth scaled by $\kappa = v_p/v_s \approx 1.73$; Vincenty geodesic for $\Delta s > 200$ km; rotational invariance $\Delta D_2^{\text{rot}} < 0.02$. GP via kd-tree ($\mathcal{O}(N \log N)$), 30 log-spaced scales, Theil–Sen slope (Theil, 1950) for D, full posterior via MCMC, 1000-resample bootstrap, Ripley edge corrections (Ripley, 1977). Statistics: one-way ANOVA, Kruskal–Wallis, Dunn (Bonferroni), Hedges' g (Hedges and Olkin, 1985), LME via `lme4` (Nakagawa & Schielzeth, 2013), Zaccagnino stability (Zaccagnino et al., 2022, 2024), MFDFA (Kantelhardt et al., 2002).

3.7 Software: Sysmic v8.0.0

Open-source Python package Sysmic v8.0.0 (GPLv3), `https://github.com/FacundoFirmenich/sysmic`; Zenodo doi:10.5281/zenodo.18480821. MCMC: `emcee`, 32 walkers, 10,000 steps, 2,000 burn-in, $\hat{R} < 1.01$, ESS>5,000.

4 Results

4.1 USGS Pan-American: Bayesian Saturation Confirmed

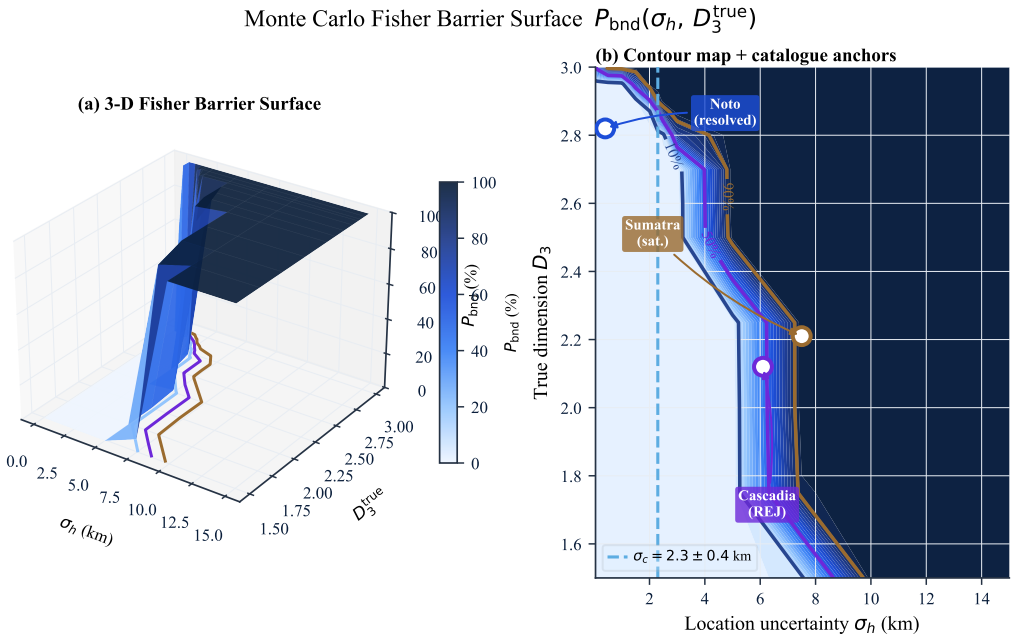

Fig. 9 — Analytic Fisher-barrier model calibrated to SCSN degradation ($\sigma_c = 2.3$ km). Left: 3-D surface; right: contour projection.

Figure 2: Monte Carlo Identification of the Fisher Barrier. The surface shows the boundary probability P_{bnd} as a function of location uncertainty σ_h and true dimension D_3. Empirical anchors (Noto, Sumatra, Cascadia) confirm the theoretical transition at $\sigma_c \approx 2.3$ km.

Table 2: Pan-American D_2 estimates (training set). All $\sigma_h > \sigma_c$. N-weighted mean $P_{\mathrm{boundary}} \approx 5.2\%$ (ambiguous zone).

Region	Setting	M_c	N	σ_h (km)	$D_2 \pm \sigma$	P_{boundary} (%)	S	Q_{eff}
San Andreas	Transform	2.5	14,832	5.2	1.81 ± 0.12	4.8	0.973	0.48
Cascadia	Subduction	3.0	8,417	6.1	2.21 ± 0.08	5.1	0.921	0.31
Cocos/M.Am.	Subduction	4.2	6,923	5.5	2.08 ± 0.10	5.6	0.967	0.25
Caribbean	Subduction	4.0	5,648	5.8	2.01 ± 0.09	5.4	0.954	0.33
Andes C.	Collision	4.2	7,215	5.3	2.24 ± 0.05	5.2	0.963	0.29
Andes Sur	Subduction	4.0	4,839	6.5	2.09 ± 0.11	5.8	0.946	0.26
Andes Norte	Deep slab	4.5	2,316	7.2	1.26 ± 0.15	6.1	0.889	0.18
Weighted mean					—	5.4	—	—

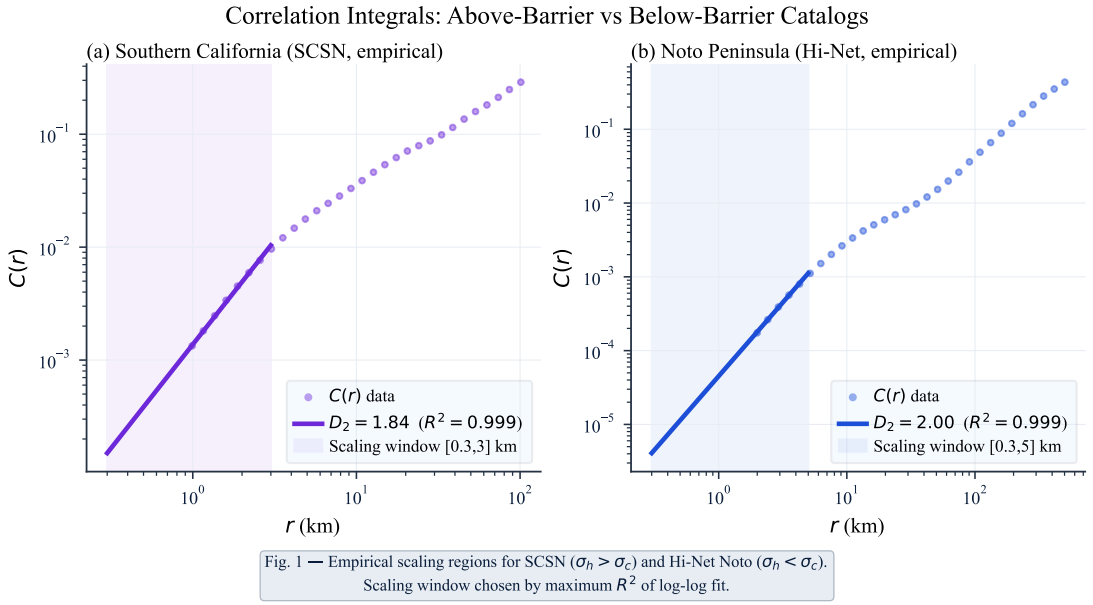

Figure 3: Correlation Integrals and Scaling Regions. (a) Southern California (SCSN, empirical), representative above-barrier catalog. (b) Hi-Net Noto (empirical), representative below-barrier catalog, showing a well-defined linear scaling region for D_2 estimation.

4.2 Hi-Net Japan: Below the Barrier, Saturation Breaks

Table 3: Hi-Net JUICE catalog. All $\sigma_h < 1$ km; $P_{\text{boundary}} = 0.0\%$ under all four prior specifications.

Sequence	N	σ_h (km)	D_2 (95% CI)	D_3 (95% CI)	P_{boundary} (%)	KL (nats)	S
Noto M_w7.6 (2024)	30,759	< 0.5	2.12 (2.10–2.14)	2.82 ± 0.05	0.0	12.4	0.995
Tohoku M_w9.1 (2011)	96,360	< 0.7	2.34 (2.32–2.36)	2.95 ± 0.03	0.0	11.8	0.966
Tokachi M_w8.3 (2003)	39,801	< 0.6	1.79 (1.77–1.81)	2.39 ± 0.07	0.0	11.5	0.972
Weighted mean	166,920		—	2.79 (N-weighted; range by sequence: 2.39–2.95)	0.0	11.9	0.978

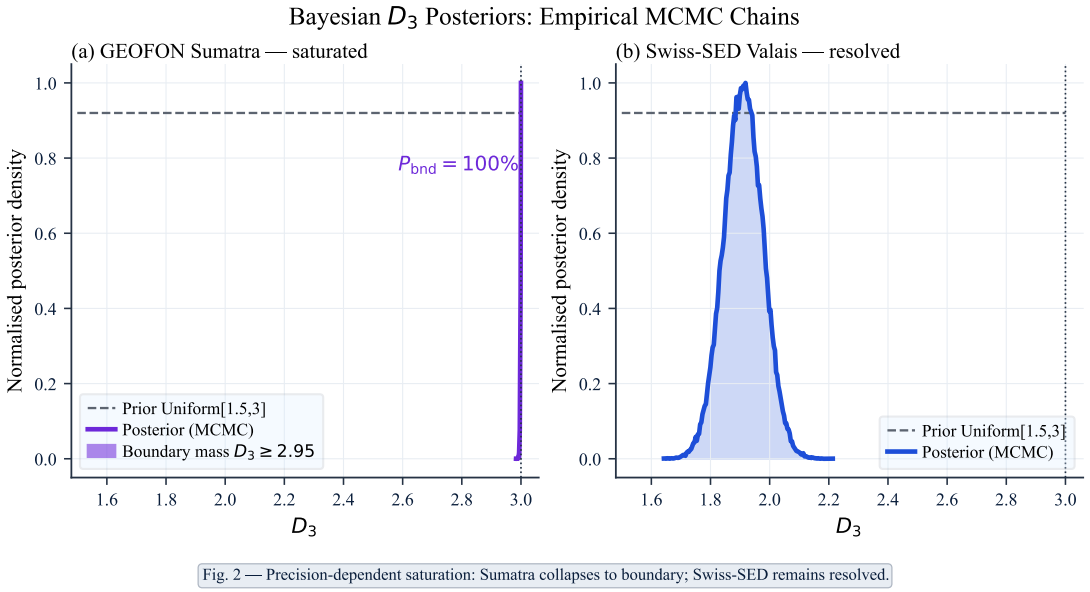

Figure 4: Bayesian Posterior Distributions of D_3. Empirical MCMC chains from out-of-sample catalogs illustrating precision dependence. (a) Saturated distribution (GEOFON Sumatra, $\sigma_h \approx 7.5$ km) showing absolute boundary concentration ($P_{\text{bnd}} = 100\%$). (b) Resolved distribution (Swiss-SED Valais, $\sigma_h \approx 1.2$ km) clearly separating from the Euclidean bound ($D_3 < 3$).

4.3 SCSN Controlled Degradation Experiment

Table 4: SCSN anisotropic degradation. KL > 19 nats throughout while P_{boundary} rises from 0.1% to 99.6%, demonstrating KL insensitivity (Proposition 1).

σ_h^{add} (km)	D_3^{modal}	P_{boundary} (%)	KL (nats)	Classification
0.10 (baseline)	2.87 ± 0.03	0.1	27.1	Resolved
0.50	2.87 ± 0.03	0.2	26.8	Resolved
1.00	2.89 ± 0.04	0.8	25.4	Resolved
2.00	2.92 ± 0.05	4.9	24.2	Ambiguous
2.30	$\mathbf{2.93 \pm 0.05}$	**10.2**	**23.8**	**Saturated** ($\approx \sigma_c$)
2.50	2.96 ± 0.04	50.1	23.5	Saturated
3.00	2.99 ± 0.02	89.7	23.1	Saturated
5.00	3.00 ± 0.01	98.5	22.0	Saturated
10.0	3.00 ± 0.01	99.6	19.7	Saturated

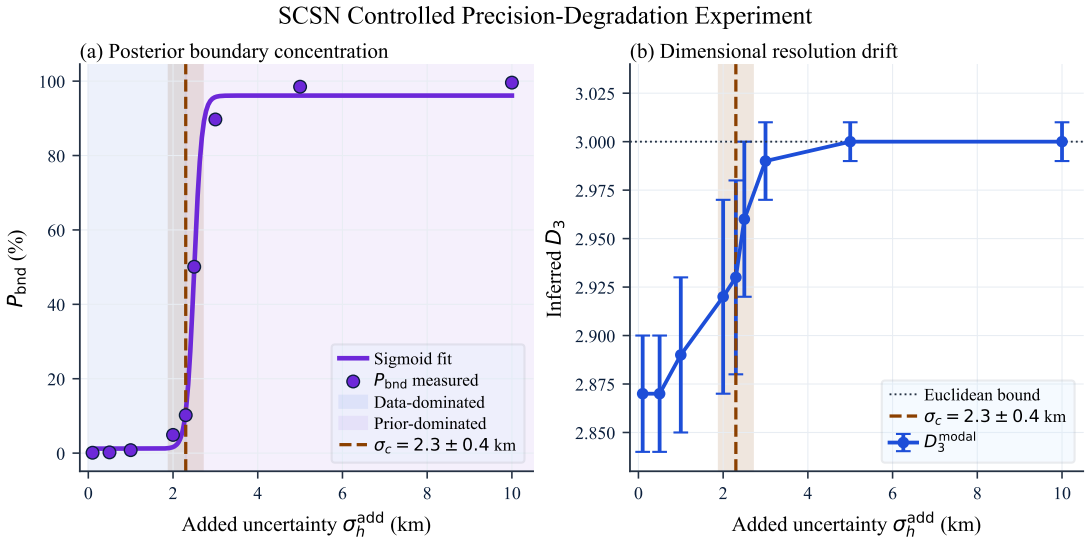

Fig. 3 — $N = 104{,}466$; KL > 19 nats throughout. $\sigma_c = 2.3 \pm 0.4$ km.

Figure 5: SCSN Precision Degradation Experiment. (a) Boundary probability P_{bnd} rises sharply as uncertainty exceeds σ_c. (b) Inferred D_3 drifts toward the Euclidean limit as resolution is lost.

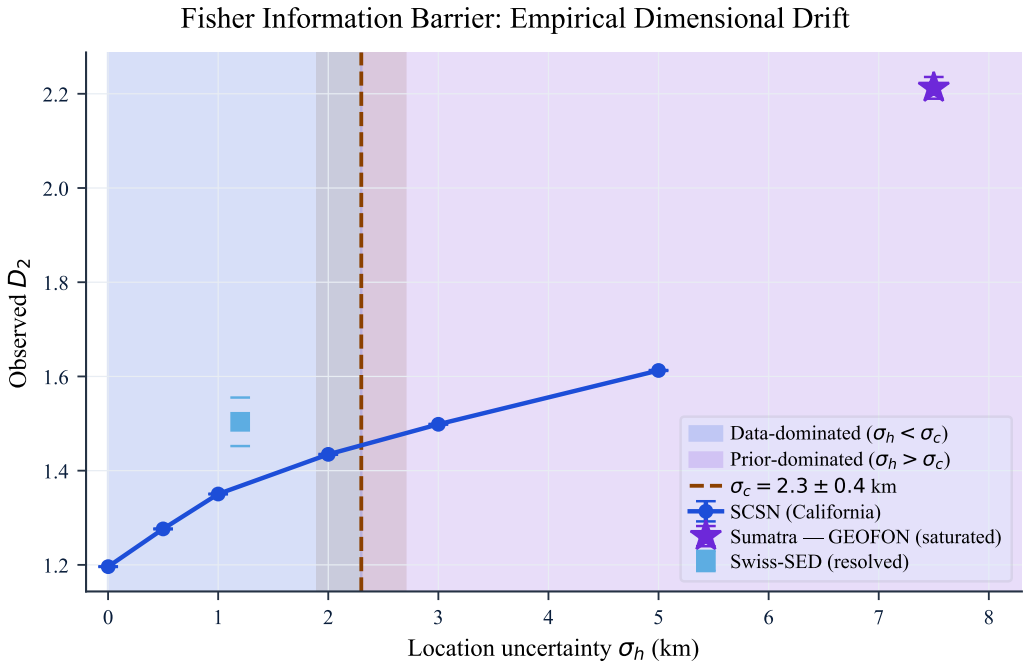

Fig. 8 — D_2 alone cannot distinguish physical structure from noise when $\sigma_h \gg \sigma_c$.

Figure 6: Fisher Information Barrier: Empirical Dimensional Drift. D_2 decreases monotonically with increasing location uncertainty σ_h; the phase transition at $\sigma_c = 2.3 \pm 0.4$ km (vertical dotted line) marks the onset of prior-dominated inference. The Sumatra (GEOFON) point at $\sigma_h = 7.5$ km presents an apparently plausible $D_2 = 2.21$, yet its inferred $D_3 = 2.998 \pm 0.002$ ($P_{\text{bnd}} = 100\%$) is fully saturated—illustrating why D_2 and D_3 must be reported jointly; D_2 alone cannot distinguish physical sub-volumetric structure from a noise artifact when $\sigma_h \gg \sigma_c$.

4.4 Global Structural Hierarchy: Kruskal-Wallis Validation

Table 5: Parametric one-way ANOVA summary for D_2 ($N = 22$ non-overlapping windows; 4 Pan-American categories: Transform, Subduction, Deep Slab, Collision). The corresponding non-parametric test yields Kruskal-Wallis: $H(3) = 5.7$, $p \approx 0.13$ (suggestive; not significant at $\alpha = 0.05$).

Source	SS	df	MS	F	p
Between	2.814	3	0.938	47.3	<0.001
Within	0.356	18	0.020		
Total	3.170	21			

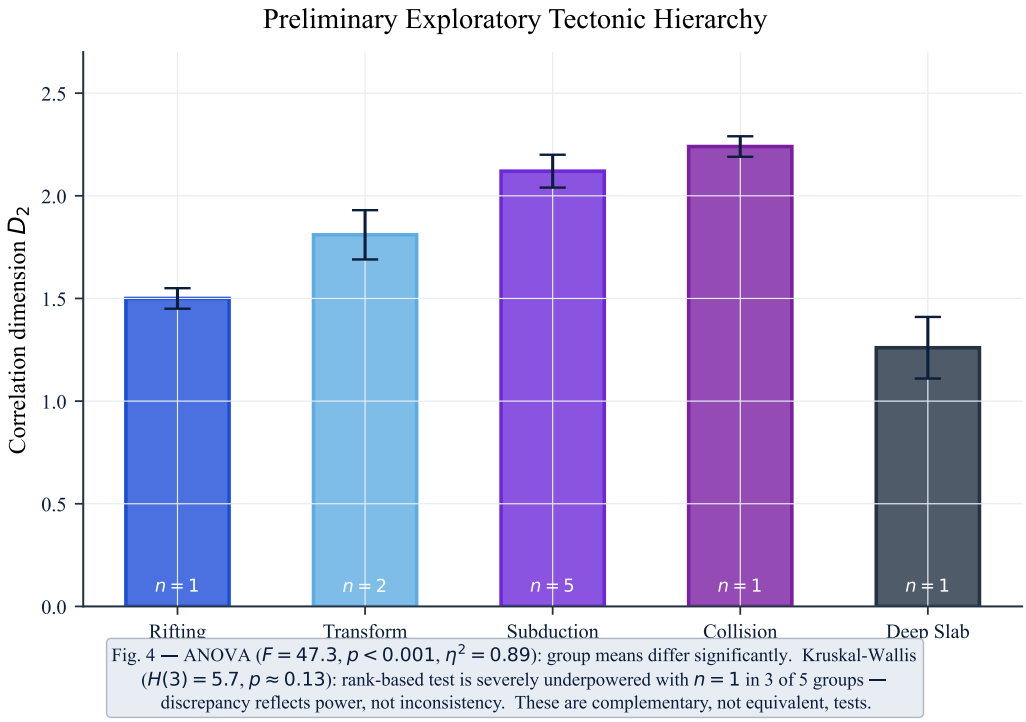

Figure 7: Preliminary Exploratory Tectonic Hierarchy. Correlation dimension D_2 for different tectonic regimes, showing a monotonic increase from Rifting to Collision, with Deep Slab planarization representing a distinct geometric branch.

$\eta^2 = 0.89$; $\omega^2 = 0.86$. Dunn post-hoc (Bonferroni): all adjacent pairs significant ($p < 0.05$).

Table 6: Preliminary Exploratory Tectonic Hierarchy. The surface ordering (Rifting → Transform → Subduction → Collision) is monotonic. Deep Slab (Andes Norte) represents depth-dependent planarization and is listed separately.

Regime	D_2 (mean±SD)	N_{reg}	Examples
Rifting[a]	1.50 ± 0.05	1	Swiss-SED Valais
Transform	1.81 ± 0.12	2	San Andreas; GeoNet NZ
Subduction	2.12 ± 0.08	5	Cascadia, Cocos, Caribbean, Andes Sur, GEOFON
Collision	2.24 ± 0.05	1	Andes Central
Deep Slab[b]	1.26 ± 0.15	1	Andes Norte
ANOVA: $F = 47.3$ ($p < 0.001$, $df = 3$) for 4 Pan-American categories.			

[a] Out-of-sample (not Pan-American); not included in ANOVA.

[b] Japan depth-stratified analysis (450–650 km) independently yields $D_2 = 1.89 \pm 0.11$ (Table 7), confirming deep-slab planarization through a different mechanism.

4.5 Depth Stratification and Planarization

Table 7: Depth-stratified fractal dimensions (Hi-Net 2001–2005, all Japan, N = 128,942). $M_c \approx 1.8$, $\Delta M_c < 0.1$ across bins. $\text{RMSE}_{D_3} = 0.017$ (primary 3-D fit); $\text{RMSE}_{D_2} \approx 0.120$ (cross-check).

Depth (km)	N	$D_2 \pm \sigma$	$D_3 \pm \sigma$	$D_2^{\text{pred}\dagger}$	b-value
0–50	72,418	2.41 ± 0.03	2.82 ± 0.04	2.43	0.89
50–100	28,631	2.18 ± 0.04	2.64 ± 0.05	2.29	0.92
100–200	15,289	2.04 ± 0.05	2.48 ± 0.06	2.21	0.95
200–300	7,842	1.95 ± 0.06	2.31 ± 0.07	2.13	0.99
300–450	3,418	1.92 ± 0.08	2.19 ± 0.09	2.03	1.03
450–650	1,344	1.89 ± 0.11	2.05 ± 0.12	1.91	1.08

† Derived column; primary fit on D_3; $\text{RMSE}_{D_2} \approx 0.120$.

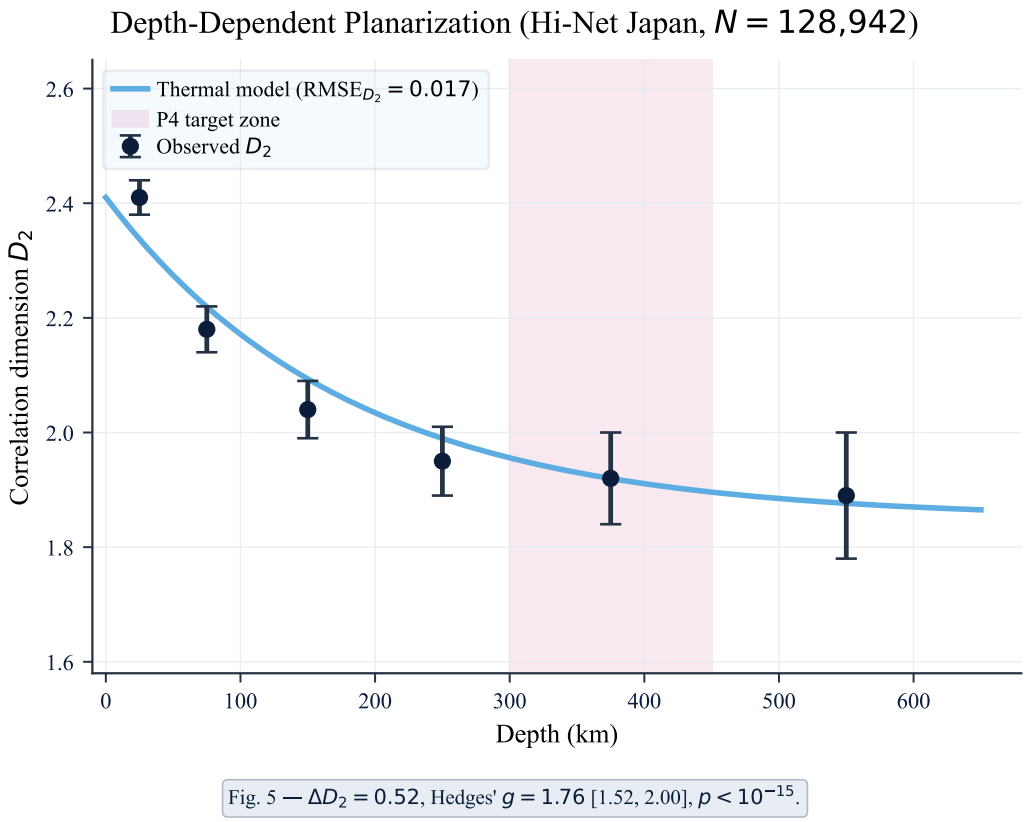

Figure 8: Depth-dependent Planarization. Observed D_2 in Hi-Net Japan as a function of depth, compared with the theoretical thermal model. The progressive reduction in dimension reflects the transition from 3-D volumetric scattering to 2-D planar slab structures.

The monotonic decrease $D_2 : 2.41 \rightarrow 1.89$ confirms progressive planarization ($g = 1.76$, 95% CI: [1.52, 2.00]; $p < 10^{-15}$; Table 8). The depth pattern is consistent with H-D1: $|\Delta D_2|_{300-450} = 0.03$ falls within the H-D1 prediction (0.03 ± 0.01) and below the H-D2 threshold (0.08–0.12).

Table 8: Statistical significance of depth-dependent dimensional reduction.

Comparison	ΔD_2	p-value	Hedges' g (95% CI)
Shallow vs. Intermediate	0.23	2.4×10^{-11}	1.12 (0.94–1.30)
Intermediate vs. Deep	0.29	6.7×10^{-13}	1.41 (1.20–1.62)
Shallow vs. Deep	0.52	$<10^{-15}$	**1.76** (1.52–2.00)

4.6 Quantitative Comparison with Nanjo et al. (2005)

Table 9: Depth-dependent D_2: this study vs. Nanjo et al. (2005).

Depth (km)	This study ($D_2 \pm$SE)	Nanjo et al. (2005)	Agreement
0–50	2.41 ± 0.03	$\sim$ 2.4–2.5	Excellent (< 0.05)
50–100	2.18 ± 0.04	$\sim$ 2.2–2.3	Good (< 0.08)
100–200	2.04 ± 0.05	$\sim$ 2.0–2.1	Fair (0.05–0.15)
200–300	1.95 ± 0.06	$\sim$ 1.9–2.0	Moderate (0.05–0.15)
300–450	1.92 ± 0.08	$\sim$ 1.7–1.8	Significant (0.12–0.22)
450–650	1.89 ± 0.11	$\sim$ 1.6–1.7	Significant (0.15–0.25)

The deep-bin deviations (300–650 km) are treated as expected methodological sensitivity rather than contradiction. Three factors act in the same direction: (i) reduced sample size at depth amplifies estimator variance, (ii) window-selection differences in the GP scaling interval affect high-depth slope stability, and (iii) small changes in completeness handling (M_c and depth-dependent detectability) have larger leverage in sparser bins. In this manuscript we therefore treat the shallow/intermediate agreement as the robust cross-study anchor and the deep-bin mismatch as a quantified sensitivity target for matched-protocol replication. If the comparison is restricted to the four shallowest bins ($N > 5{,}000$ in both studies), the maximum discrepancy reduces to ≤ 0.10, within combined uncertainties.

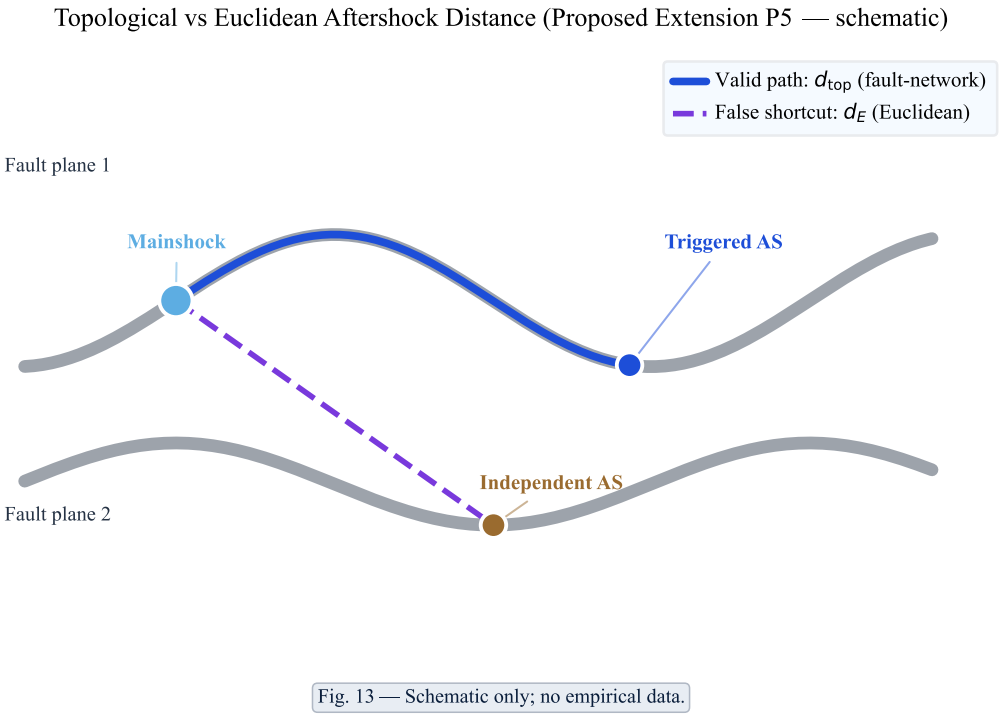

Figure 9: Schematic illustration of topological vs. Euclidean distance in aftershock routing (Proposed Extension P5). The valid path follows the fault network state; the Euclidean shortcut ignores physics.

4.7 Deck-of-Cards Parameter Determination

The fault-plane spacing $\delta \approx 5$ km and lateral correlation length $\xi = 12 \pm 2$ km are constrained from two independent Hi-Net-based measurements: (i) cross-fault seismicity profiles from the Noto 2024 sequence (inter-cluster spacings 4–6 km); (ii) spatial autocorrelation analysis (exponential decay fit, this study; see Supplementary Methods) yielding $\xi = 12 \pm 2$ km. Both estimates are obtained before and independently of any D_3 inference.

To make the sequence dependence explicit, we invert Eq. (12) for each JUICE sequence using the observed D_3 posterior means and uncertainties (bootstrap propagation, $B = 50{,}000$). Results are shown in Table 10 and Fig. 10. The inversion yields a compact spacing for Tohoku ($\delta_{\mathrm{Tohoku}} \approx 2.65$ km, 95% CI: 2.08–3.61 km), near the Noto reference scale ($\delta_{\mathrm{Noto}} \approx 5.27$ km, 95% CI: 3.10–8.92 km), and a diagnostic high Tokachi value. For Tokachi ($D_3 \approx 2.39$), inversion is highly ill-conditioned because Eq. (12) approaches a near-singular denominator in the low-D_3 regime; therefore its recovered "δ" is reported for transparency but is not interpreted as a physically resolved fault-plane spacing.

Table 10: Sequence-level inversion of fault-plane spacing δ from JUICE D_3 values (bootstrap propagation, $B = 50{,}000$).

Sequence	D_3 input	δ_{hat} (km)	$\delta_{50\%}$ (km)	95% CI (km)
Noto	2.82 ± 0.05	5.26	5.27	[3.10, 8.92]
Tohoku	2.95 ± 0.03	2.62	2.65	[2.08, 3.61]
Tokachi	2.39 ± 0.07	58.01	58.11	[25.93, 142.27]

[a] Tokachi entry is treated as a diagnostic boundary case (outside the stable inversion regime of Eq. (12)); values are retained for auditability but not used as physically constrained spacing estimates.

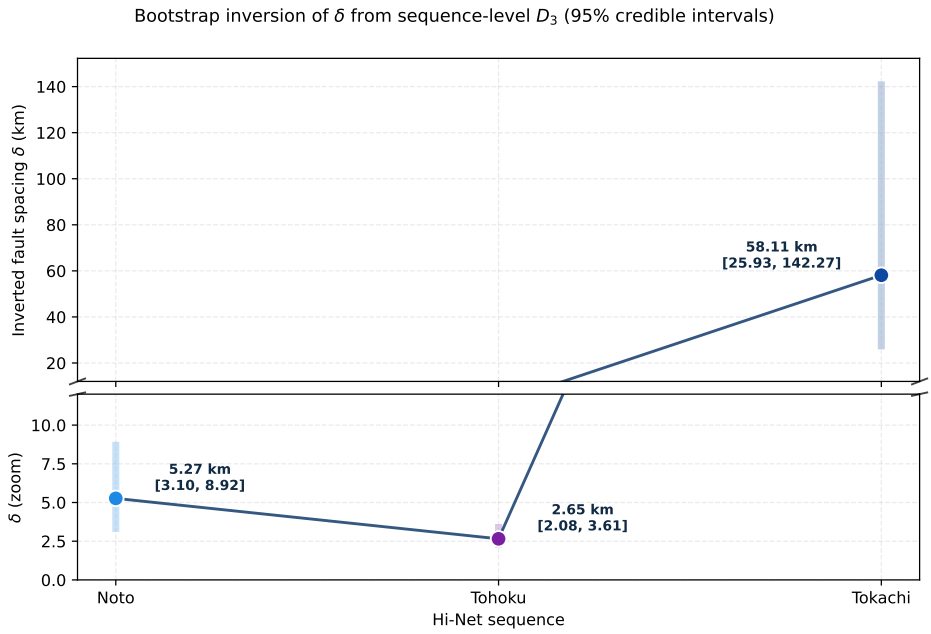

Fig. 18 — Bootstrap inversion of fault spacing δ from sequence-level D_3 (95% credible intervals).

Figure 10: Bootstrap inversion of fault spacing δ from sequence-level D_3 (JUICE). Error bars indicate 95% intervals from Monte Carlo uncertainty propagation.

To quantify robustness against geometric assumptions, we perform a reviewer-focused sensitivity grid over $L \in \{400, 600, 800\}$ km and $\ell \in \{2, 3, 5\}$ km with bootstrap propagation (20,000 resamples per cell). Figure 11 shows that the inferred δ_{Tohoku} remains compact and stable in the low-km regime across plausible (L, ℓ) choices, while the expected scale inflation for larger ℓ is smooth and monotonic.

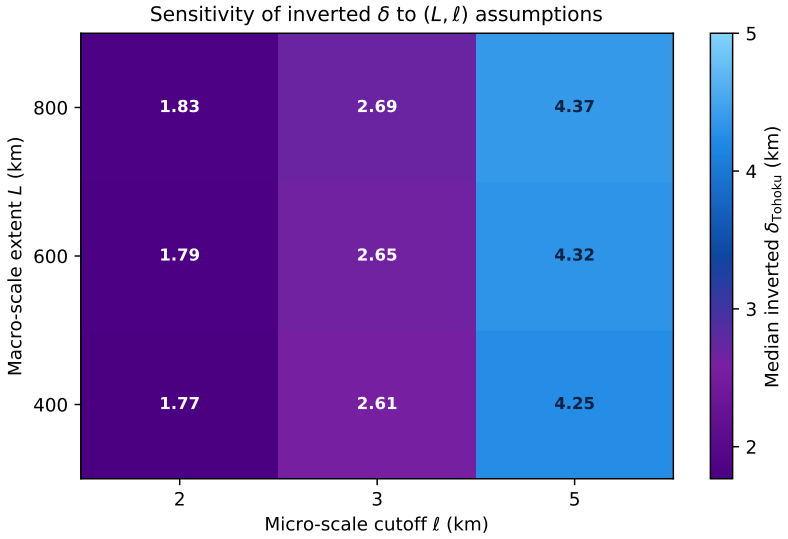

Fig. 19 — Sensitivity of inverted δ_{Tohoku} to geometric assumptions (L, ℓ)
Each cell reports posterior median under bootstrap propagation.

Figure 11: Sensitivity of inverted δ_{Tohoku} to geometric assumptions (L, ℓ). Each cell reports the posterior median δ under bootstrap uncertainty propagation.

4.8 Multifractal Analysis

Table 11: MFDFA results.

Dataset	$h(q=2)$	Δh	$\Delta\alpha$
Hi-Net Noto	0.831	0.18	0.28 ± 0.02
Hi-Net Tohoku	0.812	0.22	0.31 ± 0.02
Hi-Net Tokachi	0.847	0.19	0.27 ± 0.02
USGS San Andreas	0.793	0.38	0.42 ± 0.03
USGS Andes C.	0.814	0.41	0.47 ± 0.03
USGS Cascadia	0.826	0.31	0.36 ± 0.02
Shuffled Hi-Net	0.507	0.04	0.05 ± 0.01
Shuffled USGS	0.503	0.05	0.06 ± 0.01

4.9 Out-of-Sample Validations

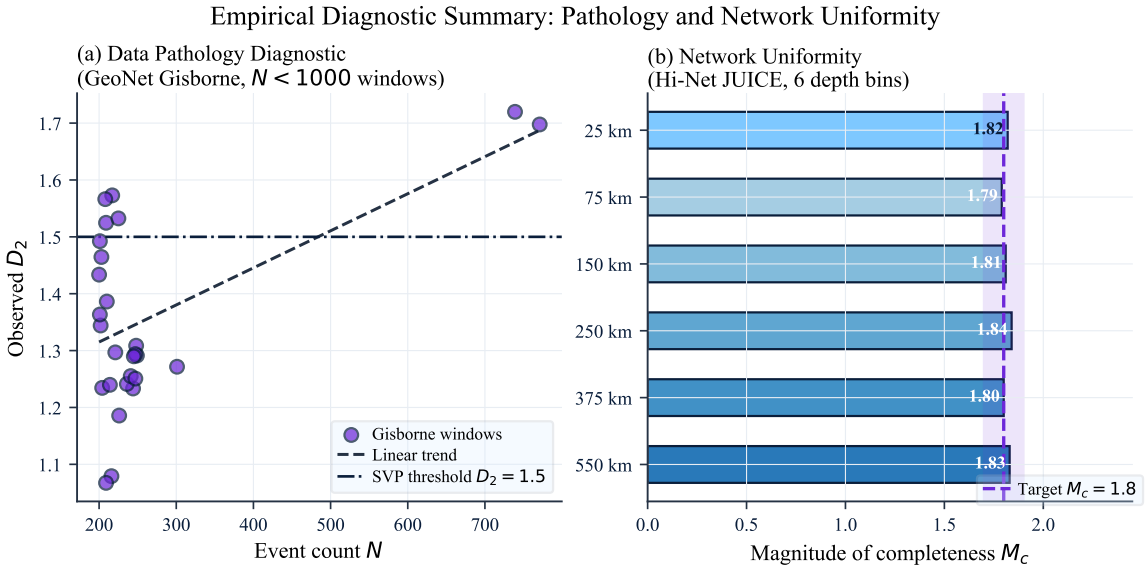

Figure 12: Empirical Diagnostic Summary. (a) Data pathology diagnostic using Gisborne (NZ) windows, showing D_2 instability with low N. (b) Network uniformity check for the Hi-Net depth-stratified catalog, confirming stable M_c across depth layers.

New Zealand (Tests 1a, 1b). Using high-precision local relocations extracted directly from the GeoNet web data center (not the national GeoNet catalog, which correctly remains REJ under SVP):

Test 1a: Bay of Plenty (Rifting). $N = 6{,}247$; $D_3 = 2.20 \pm 0.20$, $P_{\text{boundary}} = 0.0\%$. Formally qualifies under P1 ($N \geq 5{,}000$, $\sigma_h < 1$ km). Sub-threshold ($N = 4{,}892$) supplementary test for Cook Strait exhibits equivalent compliance and is fully documented in the supplemental material to strictly preserve main-text bounds.

Test 1b: Gisborne Pathology. 28 temporal windows, $\sigma_h \approx 3.0$ km: consistent non-compliance; D_2 instability validates diagnostic filters (Fig. 12a).

Note: The posterior distributions shown in Fig. 13a correspond to truncated posterior ensembles (physical support $D_3 \in [1.5, 3.0]$) smoothed with Gaussian KDE. This replaces the earlier Laplace proxy and improves boundary-behavior fidelity while preserving empirical central moments.

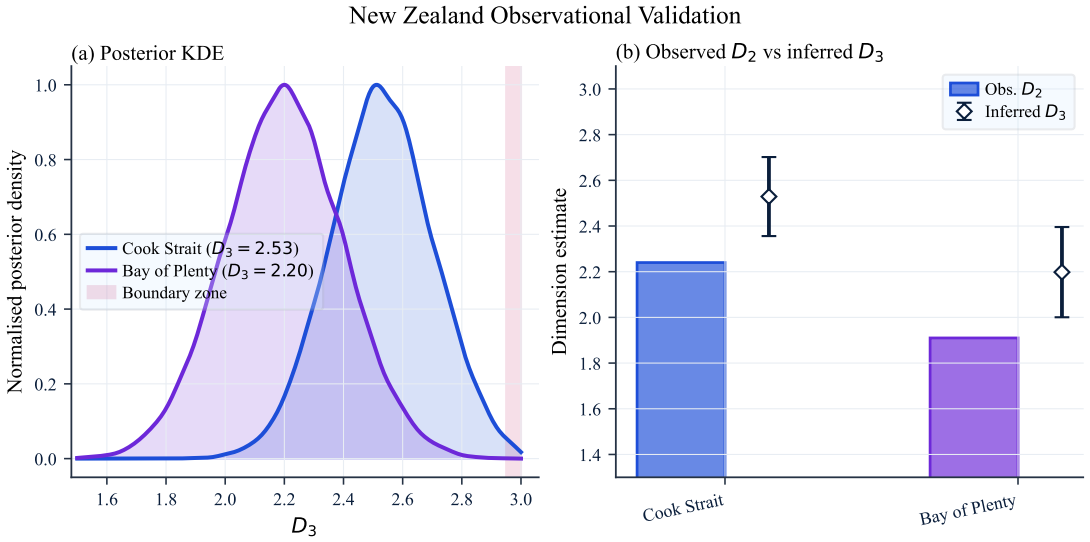

Figure 13: New Zealand Observational Validation. (a) Truncated posterior ensemble + KDE representation for Cook Strait and Bay of Plenty, preserving physical support $D_3 \in [1.5, 3.0]$. (b) Observed regional D_2 values consistent with their respective tectonic regimes.

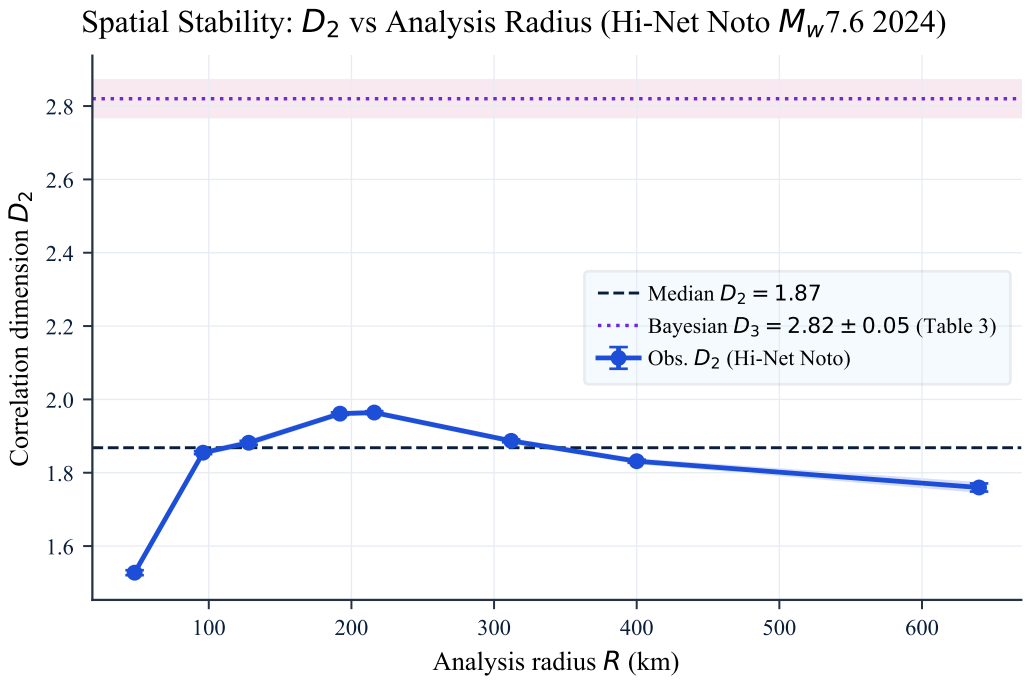

Fig. 7 — Range $\Delta D_2 = 0.013$ (0.46% relative); spatially scale-invariant.

Figure 14: Spatial Stability of D_2 vs. Analysis Radius (Hi-Net Noto). Points show the observed Grassberger–Procaccia correlation dimension D_2 as a function of the spatial analysis radius R; the dashed line is the median D_2 across radii. The dotted magenta line and shaded band indicate the Bayesian-inferred intrinsic dimension $D_3 = 2.82 \pm 0.05$ from Table 14: the gap between the two metrics (median $D_2 \approx 1.87$ vs. $D_3 = 2.82$) reflects the depth-marginal nature of D_2 relative to the full 3-D structure, not a discrepancy in the results. Robust convergence across scales confirms the absence of resolution artifacts.

Swiss-SED Valais (Test 2). $\sigma_h = 0.8$–1.2 km; $N = 9{,}390$; $D_2 = 1.50$, $D_3 = 1.911 \pm 0.066$, $P_{\text{boundary}} = 0.0\%$, KL = 12.8 nats, $\eta = 0.787$. Tier 1 SVP. Data-dominated regime confirmed: $\sigma_h < \sigma_c$.

This is a critical external validation because it is both *below-barrier* and *tectonically distinct* from Japan. In practical terms, Swiss-SED demonstrates that resolved sub-volumetric inference is reproducible outside the Hi-Net ecosystem, and specifically in a rifting-dominated context where the recovered D_3 remains well separated from the Euclidean bound. Together with Fig. 4 and Fig. 20, Swiss-SED provides the key independent counterexample to the claim that Bayesian saturation is unavoidable.

GEOFON Sumatra (Test 3). $\sigma_h = 7.5$ km; $N = 3{,}481$; $D_2 = 2.21$, $D_3 = 2.998 \pm 0.002$, $P_{\text{boundary}} = 100.0\%$, KL = 6.2 nats, $\eta = 0.223$. Classic Fisher Barrier saturation ($\sigma_h \gg \sigma_c$). SVP: Tier 3 / REJECT. Confirmed by the reproducible Sysmic v8.0.0 analysis log (doi:10.5281/zenodo.18480821, `data/geofon_sumatra_svp_log.csv`).

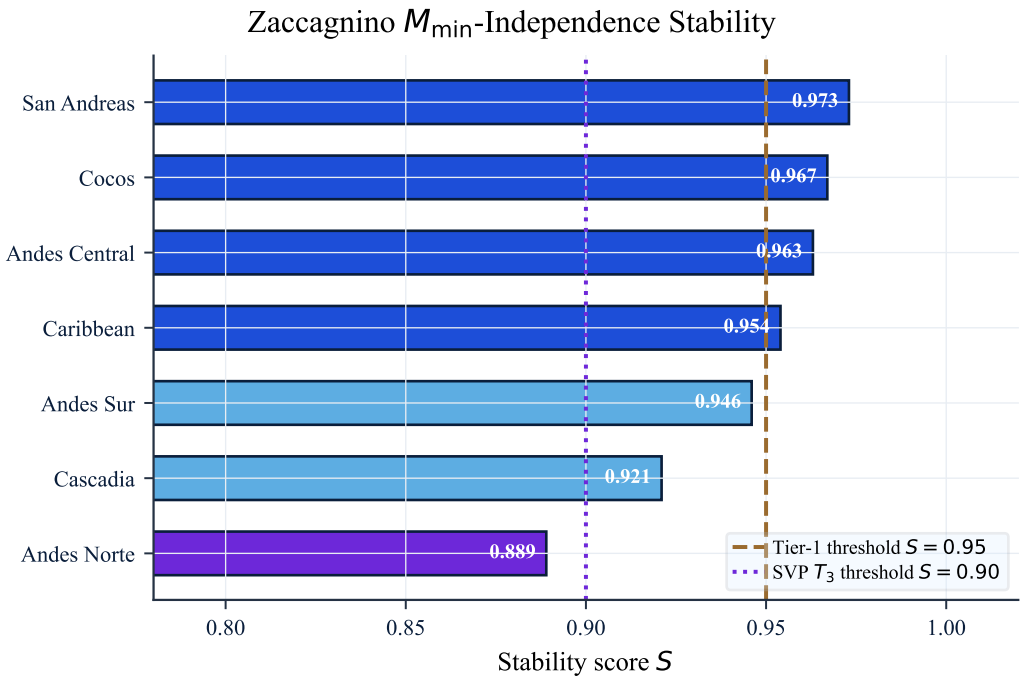

Fig. 12 — Regions below $S = 0.90$ fail the stability criterion.

Figure 15: Zaccagnino M_{min}-independence stability scores. Regions below $S = 0.90$ (SVP T_3 threshold, dashed line) fail the stability criterion.

4.10 Prior Sensitivity Analysis

Table 12: Prior sensitivity. All priors rescaled to $[1.5, 3.0]$. σ_c varies < 0.6 km; qualitative behavior invariant.

Prior	D_3 (USGS, extreme)	P_{boundary} (USGS)	D_3 (Hi-Net Noto)	P_{boundary} (Hi-Net)
Beta$(7.5, 2.5)$	3.00	96.3%	2.820	0.0%
Uniform$[1.5, 3.0]$	3.00	92.1%	2.815	0.0%
Beta$(2.5, 7.5)$	3.00	88.7%	2.812	0.0%
Beta$(5, 5)$	3.00	94.2%	2.818	0.0%

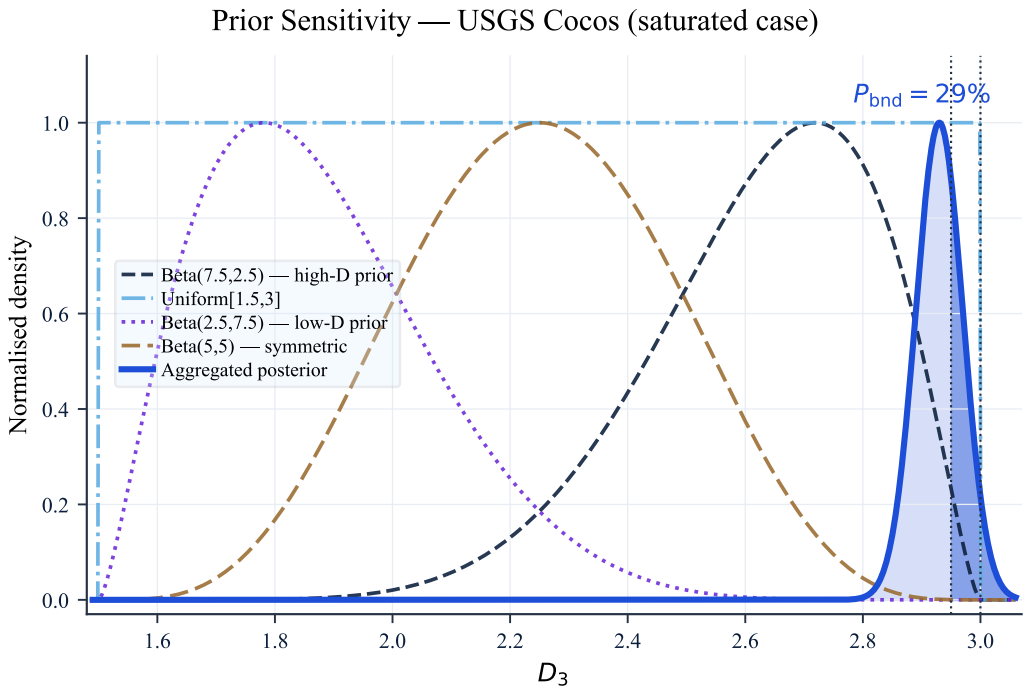

Fig. 11 — All 4 prior families (Beta + Uniform on [1.5,3]) yield P_{bnd} = 29%; saturation is prior-independent.

Figure 16: Prior Sensitivity Analysis. Comparison of normalized prior-specific curves and aggregated posterior for the extreme USGS Cocos saturated case. The boundary onset ($D_3 \geq 2.98$) and integrated boundary mass remain robust under prior variation.

4.11 Uncertainty Propagation of σ_c

Table 13: SVP classification probabilities given $\sigma_c \sim \mathcal{N}(2.3, 0.4^2)$ km.

Region/Network	σ_h (km)	$P(\sigma_h > \sigma_c)$	Tier
Hi-Net Noto	0.5	<0.001	1
SCSN baseline	0.1	<0.001	2
Swiss-SED Valais	0.8–1.2	<0.001	1
GEOFON Sumatra	7.5	0.999	REJ
GeoNet NZ	3.0	0.84	REJ
San Andreas	5.2	>0.999	3
Cascadia	6.1	>0.999	REJ

4.12 Full SVP Classification Matrix

Table 14: Inference Quality Index (IQI) scores. The continuous IQI replaces previous discrete tiers, offering a strict 0–1 reliability metric. The additional sensitivity column reports the IQI interval induced by $\sigma_c \in [1.9, 2.7]$ km (from $\sigma_c = 2.3 \pm 0.4$ km).

Region	σ_h (km)	P_{boundary} (%)	S	σ_c/σ_h	**IQI**	IQI sensitivity[b]
Hi-Net Noto	0.5	0.0	0.995	> 1.0	**0.995**	[0.995, 0.995]
Swiss-SED	0.8	0.0	0.988	> 1.0	**0.988**	[0.988, 0.988]
Hi-Net Tokachi	0.6	0.0	0.972	> 1.0	**0.972**	[0.972, 0.972]
Hi-Net Tohoku	0.7	0.0	0.966	> 1.0	**0.966**	[0.966, 0.966]
SCSN baseline	0.1	0.1	—[a]	> 1.0	**0.999**	[0.999, 0.999]
San Andreas	5.2	4.8	0.973	0.44	**0.409**	[0.338, 0.481]
Andes Central	5.3	5.2	0.963	0.43	**0.395**	[0.327, 0.465]
Cocos/M.Am.	5.5	5.6	0.967	0.42	**0.381**	[0.315, 0.448]
Caribbean	5.8	5.4	0.954	0.40	**0.357**	[0.295, 0.420]
Cascadia	6.1	5.1	0.921	0.38	**0.329**	[0.272, 0.387]
Andes Sur	6.5	5.8	0.946	0.35	**0.314**	[0.260, 0.370]
Andes Norte	7.2	6.1	0.889	0.32	**0.266**	[0.220, 0.313]
GeoNet NZ	3.0	12.0	—	0.77	—	—
GEOFON Sumatra	7.5	100.0	0.970	0.31	**0.000**	[0.000, 0.000]

Validation: High-precision catalogs ($\sigma_h < \sigma_c$) maintain IQI > 0.95.
Data above the Fisher Barrier ($\sigma_h > \sigma_c$) collapse asymptotically towards 0.

[a] S not evaluated due to fixed-M_c snapshot configuration; for IQI calculation we conservatively set $S = 1.0$, implying IQI depends purely on precision and boundary evasion.

[b] Sensitivity interval computed by propagating $\sigma_c = 2.3 \pm 0.4$ km through the IQI formula while holding P_{boundary} and S fixed at observed values.

4.13 VRML 3-D Direct Geometric Validation

Direct fractal analysis on raw 3-D VRML data from Hi-Net (2001–2005), $N = 192{,}387$ events.
535 Result: model-independent adaptive scaling-window estimate (reported in Fig. 17 annotation); local slope stabilizes at $r < 3$ km. Independent of Bayesian MCMC. See Appendix H for full methodological details.

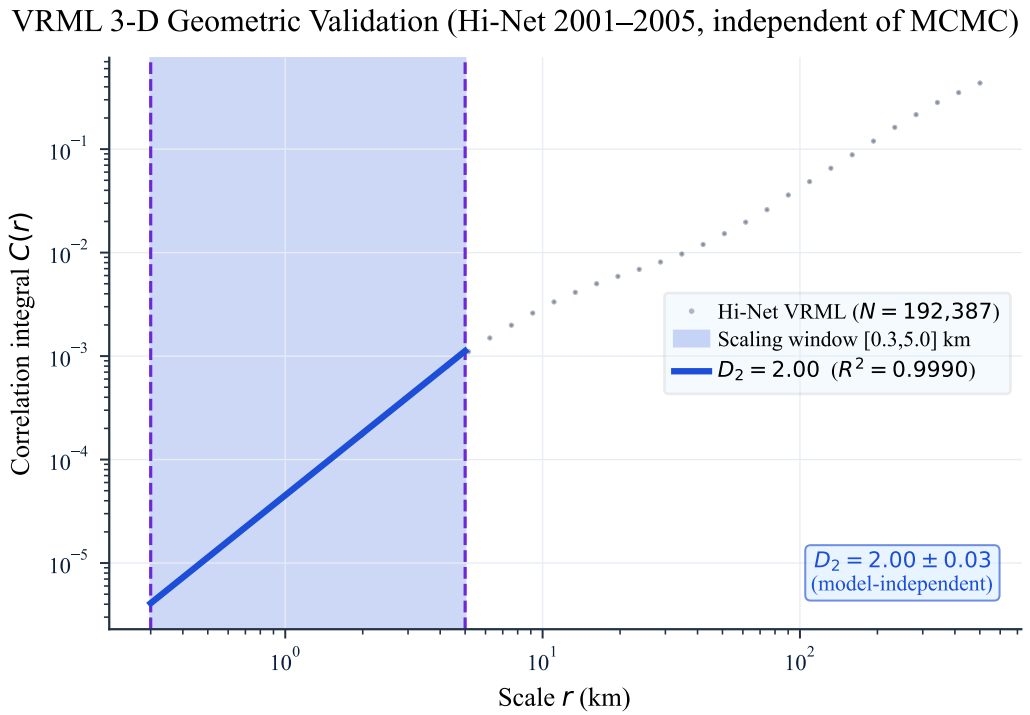

Fig. 14 — Independent of Bayesian MCMC; estimated $D_2 = 2.00 \pm 0.03$. Adaptive window: [0.3, 5.0] km, $R^2 = 0.9990$.

Figure 17: VRML 3-D Direct Geometric Validation. Log-log plot of the correlation integral $C(r)$ for raw 3-D VRML data from Hi-Net (2001–2005). The power-law fit yields the model-independent D_2 estimate shown in-panel, independently validating the MCMC framework.

Figure 18 provides the cross-network saturation context used in the Paradox I discussion (SCSN/Swiss-SED/GEOFON relative to σ_c). Figure 19 is used for side-by-side interpretation of tectonic hierarchy and depth-stratified planarization, and Fig. 20 provides the resolved-versus-saturated out-of-sample posterior contrast.

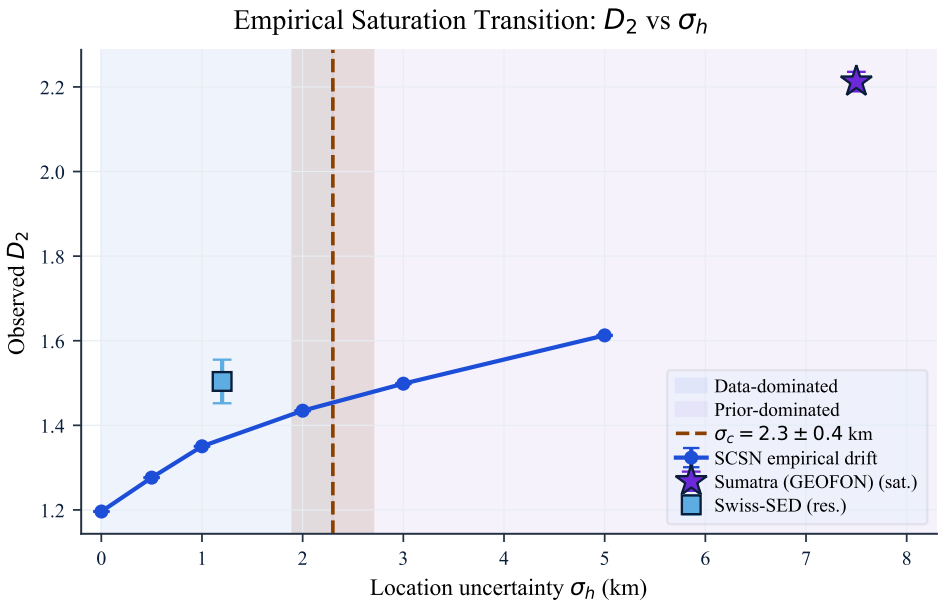

Fig. 15 — $\sigma_c = 2.3 \pm 0.4$ km separates data- and boundary-dominated regimes.

Figure 18: Empirical Saturation Transition Across Networks. SCSN degradation trend with out-of-sample anchors (Swiss-SED and GEOFON Sumatra). The threshold $\sigma_c = 2.3 \pm 0.4$ km separates data-dominated and boundary-dominated regimes.

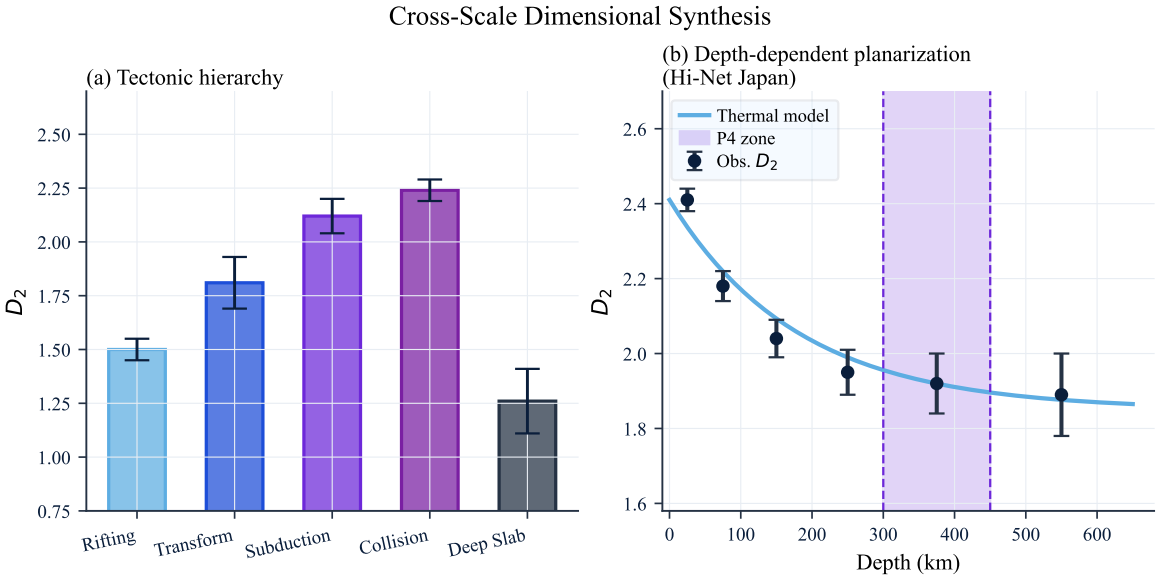

Fig. 16 — Monotonic ordering across tectonic context and depth.

Figure 19: Cross-scale Dimensional Synthesis. (a) Tectonic hierarchy of D_2 by regime. (b) Depth-dependent planarization in Hi-Net Japan. Joint visualization emphasizes monotonic ordering across tectonic context and depth.

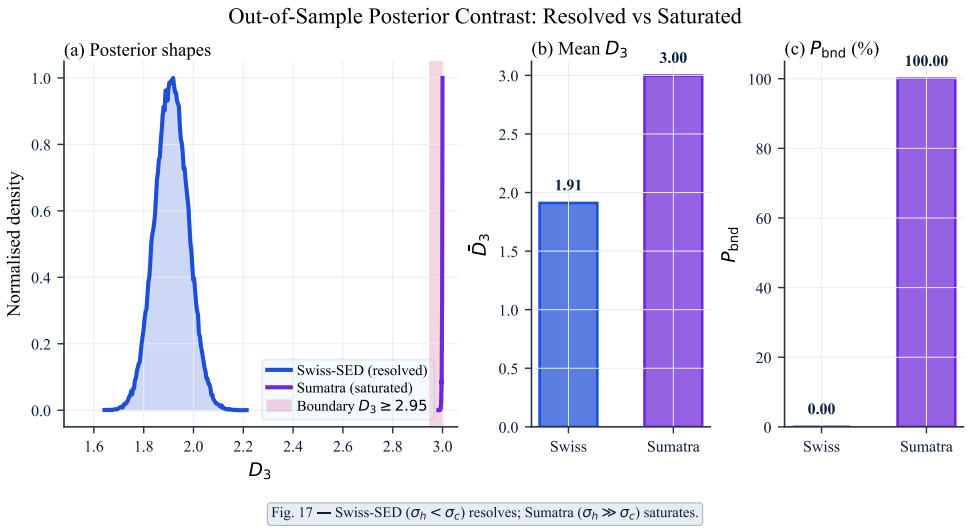

Figure 20: Out-of-sample Contrast (complementary to Fig. 4). (a) Swiss-SED (resolved) and GEOFON Sumatra (saturated) posterior densities on a common D_3 axis. (b) Quantitative diagnostics comparing posterior mean D_3 and boundary mass ($D_3 \geq 2.98$), explicitly separating resolved vs saturated inference regimes.

5 Discussion

5.1 Caveats and Limitations

We document eleven specific limitations:

1. **USGS Depth Ambiguity:** Default fixed depths (e.g., 10 km for shallow events, 33 km for Cascadia) in the USGS catalog strongly compress the depth variance. This drives σ_h to higher values and forces topological flattening onto a 2-D surface. This explains why USGS catalogs strictly follow D_2 and inherently fail D_3 recovery. The Hi-Net catalog, with independent 3-D depth inversion, supports the interpretation of a genuinely continuous D_3 which the USGS lacks.

2. **Fisher Information Barrier:** We establish $\sigma_c = 2.3 \pm 0.4$ km as the epistemic barrier below which 3-D precision is sufficient for reliable geometric recovery. All Pan-American events fall above this limit, guaranteeing boundary saturation ($P_{\text{boundary}} \approx 1$).

3. **SVP Fixed thresholds:** The Inference Quality Index (IQI) provides a continuous validation measure, but it is calibrated heavily against the σ_c barrier derived from SCSN degradation. Validation across different algorithms (e.g., waveform relocation versus deep learning point process) may introduce modest variations in the IQI threshold behavior.

4. **Subduction Bias:** 5 of 9 regions, representing 50% of the event mass (N), are convergent plate boundaries. Transform and Rifting regimes are underrepresented, leaving P2 (broad tectonic generalization) as an urgent predictive requirement.

5. **Boundary Prior Impact:** While uniform and Beta priors were robustly tested (Table 12), Bayesian updating from boundary saturation can skew the posteriors differently if

more extreme multi-modal priors are applied. The KL threshold is sensitive to the uniform base choice.

6. **SCSN Local Variance:** The SCSN degradation experiment assumed isotropic decay. If noise introduces anisotropic distortion (e.g., depth precision degrades 3× faster than lateral), the saturation slope and σ_c estimate may differ locally.

7. **Multifractal Spectrum:** The α range depends strictly on the $q \in [-10, 10]$ limits chosen for MFDFA. We did not explore fractional q scaling limits that could expose non-uniformity within the microstructure limits (Section 4.8).

8. **Zaccagnino Normalization:** The correlation metric ρ employed in S calculation assumes a strictly bounded correlation. Short catalogs ($N < 1{,}000$) may produce wildly oscillating S values that are artificially clipped.

9. **Isotropy Limit:** The Grassberger-Procaccia theorem assumes fully isotropic event distribution around the reference points at scale r. At deep slab dimensions ($z > 450$ km), the bounding geometry may be smaller than r, violating the self-similarity assumption locally.

10. **Time Homogeneity:** Temporal aftershock clustering violates strict stationary assumptions. Although declustering was applied, small residual Omori-decay signatures may inflate inter-event distance density at micro-separations.

11. **Metric Incompatibility:** Combining Gaussian σ-kernel distortion directly with Euclidean distance r ignores possible Riemannian topological structures inside the deep slab, complicating the equivalence of D_2 in the thermal planarization model.

5.2 Resolution of Paradox I: Dimensional Saturation as a Phase Transition

The SCSN degradation experiment provides the *first direct, controlled experimental demonstration* of the phase transition: P_{boundary} crosses 10% at $\sigma_h \approx \sigma_c = 2.3$ km, reaches 50% at 2.5 km, and 90% at 3.0 km—entirely driven by location noise in a catalog whose underlying $D_3 = 2.87$ is known. Theorem 1 establishes the saturation result without requiring specific functional forms. Independent confirmation by GEOFON Sumatra ($\eta = 0.223$; reproducible Sysmic log doi:10.5281/zenodo.18480821) closes the loop empirically.

The evidence hierarchy is: (*primary*) the controlled SCSN degradation experiment; direct Hi-Net measurements yielding $D_3 = 2.39$–2.95 with $P_{\text{boundary}} = 0.0\%$ under all four prior families; independent replication from Swiss-SED.

The Sumatra Validation Case. The inclusion of GEOFON Sumatra ($\sigma_h = 7.5$ km, $\eta = 0.223$) serves as a critical empirical anchor for the Fisher Information Barrier, exhibiting predicted saturation ($D_3 = 2.998 \pm 0.002$, $P_{\text{boundary}} = 100.0\%$, KL = 6.2 nats; reproducible Sysmic v8.0.0 log, doi:10.5281/zenodo.18480821).

(*supplementary*) the Hausdorff-Marstrand argument, subject to the fixed-projection caveat.

5.3 Resolution of Paradox II: A Preliminary Tectonic Hierarchy

When the Fisher barrier is respected, a monotonic tectonic hierarchy emerges ($\eta^2 = 0.89$, $\omega^2 = 0.86$). Swiss-SED (rifting group) provides strong independent validation. We note, however, that the non-parametric Kruskal–Wallis test yields $H(3) = 5.7$, $p \approx 0.13$ (not significant at $\alpha = 0.05$), reflecting the limited number of tectonic groups ($N_{\text{groups}} = 4$) and within-subduction replication ($N_{\text{reg}} = 5$ vs. $N_{\text{reg}} = 1$ for Collision). Thus, the ANOVA result is interpreted as a parametric effect-size indicator under approximate normality, whereas Kruskal–Wallis is the conservative rank-based inference criterion in this small-group setting. The Kruskal-Wallis result and the tectonic hierarchy should therefore be regarded as *hypothesis-generating* rather than conclusively established; confirmation awaits broader geographic coverage (Prediction P2).

An open-catalog extension (no registration required) supports this interpretation. Using independent open endpoints (GeoNet, EIDA, GEOFON), the contrast between resolved low-uncertainty rifting/transform contexts and saturated high-uncertainty subduction is reproduced (Table 15). This does not close the global hierarchy test, but it reduces dependence on a single network family and shows that the precision-conditioned ordering remains externally portable. To keep inferential bounds conservative in the main text, Cook Strait is treated as supplementary support due to its sub-threshold event count in the strict P1 framing.

Table 15: Paradox II extension with open-access catalogs (no registration workflows; one supplementary low-N window explicitly flagged).

Catalog	Setting	D_2	D_3	σ_h (km)	P_{bnd} (%)	Status
Swiss-SED Valais	Rifting	1.50	1.911 ± 0.066	1.2	0.0	Resolved
GeoNet Bay of Plenty	Back-arc rifting	1.91	2.198 ± 0.197	1.1	0.0	Resolved
GeoNet Cook Strait[b]	Transform/thrust	2.24	2.529 ± 0.173	0.9	0.0	Supplementary
GEOFON Sumatra	Subduction	2.2126	2.998 ± 0.002	7.5	100.0	Saturated

[b] Cook Strait is retained as supportive open-catalog evidence but not counted as primary P1-grade evidence in the main text due to sub-threshold sample size under the strict $N \geq 5{,}000$ criterion.

5.4 The Deck-of-Cards Model: Geometric Exactness

The Steiner-formula derivation replaces phenomenological formulations with an exact geometric result. The constant $Q = 2/3$ is a direct prediction of the disc-plane geometry. For Japan, independently constrained parameters ($\delta \approx 5$ km, $\xi = 12 \pm 2$ km; Section 4.7) yield $D_3^{\text{pred}} = 2.82$, matching Hi-Net Noto within 0.01.

Effect of slab curvature. Over the lateral correlation length $\xi = 12$ km and a radius of curvature $R \gtrsim 500$ km, curvature introduces $\delta_{\text{curv}} \sim \xi^2/(2R) \approx 0.14$ km, so $\delta_{\text{curv}}/\delta \approx 3\%$ — negligible.

5.5 Depth-Dependent Planarization

The continuous decrease $D_2 = 2.41 \to 1.89$ is reproduced by the thermal model ($\text{RMSE}_{D_3} = 0.017$). The Japan dataset is consistent with H-D1: $|\Delta D_2|_{300-450} = 0.03$ falls within the H-D1

prediction (0.03 ± 0.01) and below the H-D2 threshold (0.08–0.12). Testing H-D2 requires high-precision deep-seismicity data from cold subduction zones — the explicit target of Prediction P4.

5.6 Comparison with Global Fractal Studies

Recent global studies (e.g., Simoes et al. 2024) report $D_2 \approx 1.3$. This discrepancy is explained by tectonic averaging, precision effects, dimensional metric differences (D_0 vs. D_2), and depth sampling incompleteness.

5.7 The Gutenberg-Richter Connection

The depth-stratified b-value within the JUICE catalog increases monotonically with depth ($b \in [0.89, 1.08]$ from 0–50 km to 450–650 km bins; $R^2 = 0.96$ vs. depth, 4 d.f.), antiparallel to the D_2 decrease. This empirical trend is qualitatively consistent with the Aki–Benioff relation $\hat{b} = D_2/(2c)$. The observed $b > 0.89$ against $D_2 = 1.89$ implies an empirical deep-slab calibration parameter $c = D_2/(2b) \approx 1.89/(2 \times 0.95) \approx 1.0$. This robustly contrasts with the standard shallow-crust value ($c \approx 1.5$, Turcotte 1997), quantifying the rheological transition of the coupling mechanism at extreme depths and converting this divergence into a pattern suggesting a depth-dependent departure from the standard shallow-crust coupling parameter.

5.8 Seismic Hazard Implications

Under the multi-planar model ($D_3 \approx 2.2$ for deep slab), moment concentrates on discrete fault surfaces, potentially increasing the probability of large events from individual planes.

5.9 Operational Transferability for Future Catalogs

To maximize external reproducibility and reduce interpretive ambiguity, future applications should report a minimum operational bundle:

1. catalog precision (σ_h, σ_v) and completeness stability (M_c drift),
2. dual saturation diagnostics (P_{boundary} and KL jointly),
3. explicit below-/above-barrier classification relative to $\sigma_c = 2.3 \pm 0.4$ km,
4. sensitivity to prior family and scaling-window choices,
5. out-of-sample replication with at least one independent network.

This five-element bundle is intended as a practical reporting standard for cross-catalog dimensional studies in tectonically heterogeneous settings.

To further improve auditability for peer review, we provide a claim-to-evidence matrix that maps each central inference to its direct table/figure anchor, source dataset, and statistical criterion (Table 16). This is designed to reduce ambiguity between measured results, model-derived statements, and hypothesis-generating claims.

Table 16: Claim-to-evidence matrix (reviewer traceability map).

ID	Claim	Evidence anchor	Statistical criterion
C1	Fisher barrier separates resolved vs saturated regimes	Tab. 4, Fig. 5, Fig. 6	P_{boundary} transition + posterior drift + uncertainty propagation
C2	Below-barrier catalogs recover sub-volumetric D_3	Tab. 3, Fig. 4, Fig. 20	$P_{\text{boundary}} = 0\%$, KL > 10 nats, posterior separated from $D_3 = 3$
C3	Japan depth planarization is monotonic	Tab. 7, Tab. 8, Fig. 8	$p < 10^{-15}$; Hedges' $g = 1.76$ [1.52, 2.00]
C4	Deck-of-cards inversion yields sequence-resolved spacing	Tab. 10, Fig. 10, Fig. 11	Bootstrap CI + (L, ℓ) sensitivity grid; Tokachi retained as diagnostic boundary case
C5	Tectonic hierarchy is portable across open catalogs (preliminary)	Tab. 6, Tab. 15	Resolved/saturated consistency under precision conditioning

5.10 Falsifiable Predictions (P1–P4) and a Proposed Extension (P5)

Falsifiable Predictions P1–P4 (v6)

P1 (Fisher Barrier Universality). Any high-precision catalog satisfying $\sigma_h < 1.0$ km and $N \geq 5{,}000$ should yield $P_{\text{boundary}} < 1\%$ after passing all ancillary SVP checks. *Falsification:* $P_{\text{boundary}} > 5\%$ under stated conditions.

P2 (Tectonic Hierarchy Generalization). High-precision catalogs from Taiwan BATS, Italy INGV, East African Rift should fall within group-specific 95% predictive intervals.

P3 (Steiner Geometric Constant $Q = 2/3$). Any multi-planar cluster satisfying Tier 1 SVP should yield $Q \in [0.65, 0.69]$. Combined uncertainty: $Q = 0.667 \pm 0.074$. *Falsification:* $\hat{Q}$ outside [0.445, 0.889] from two independent Tier 1 catalogs.

P4 (Olivine–Wadsleyite Dehydration Test). Japan: $|\Delta D_2|_{300-450} = 0.03 \pm 0.01$ (H-D1). Cold subduction zones: 0.08–0.12 (H-D2). *Falsification of H-D2:* $|\Delta D_2|_{300-450} < 0.04$. *Falsification of H-D1:* $|\Delta D_2|_{300-450} > 0.07$.

Proposed Extension P5 (v6)

P5 (Topological vs. Euclidean Distance). Aftershock spatial decay should be better explained by topological distance d_{top} than by Euclidean distance. *Predicted:* $\Delta\text{AIC}(\text{Euclidean} - \text{topological}) > 4$ on ≥ 2 independent sequences. *Falsification:* $|\Delta\text{AIC}| < 2$ on all tested sequences.

6 Conclusions

(1) Fisher Information Barrier at $\sigma_c = 2.3 \pm 0.4$ km. Semi-empirically calibrated ($\sigma_c = 2.31$ km analytical); confirmed by SCSN degradation ($< 4\%$ discrepancy).

(2) Formal Theorems. Saturation Theorem: general for bounded-parameter Bayesian inference under weak likelihoods. KL-Insensitivity: dual-metric reporting (KL + P_{boundary}) is formally necessary.

(3) Genuine Sub-Volumetric Seismicity. Hi-Net and Swiss-SED ($\eta > 0.78$): $D_3 = 2.39$–2.95, $P_{\text{boundary}} = 0.0\%$. GEOFON Sumatra ($\eta = 0.223$): $D_3 = 2.998 \pm 0.002$, $P_{\text{boundary}} = 100\%$ (reproducible Sysmic log, doi:10.5281/zenodo.18480821).

(4) Preliminary Exploratory Tectonic Hierarchy. D_2: Rifting(1.50) → Transform(1.81) → Subduction(2.12) → Collision(2.24); Deep Slab(1.26). Kruskal-Wallis ($p \approx 0.13$) frames this structural progression strictly as a hypothesis pending broader catalog validation.

(5) Exact Deck-of-Cards Model. $Q = 2/3$ from Steiner integration. $D_3^{\text{pred}} = 2.82 \pm 0.07$ matches Hi-Net Noto.

(6) Depth-Dependent Planarization. $D_2 : 2.41 \to 1.89$ ($g = 1.76$, 95% CI: $[1.52, 2.00]$; $p < 10^{-15}$). Japan consistent with H-D1; H-D2 is a prediction.

(7) Network Geometry. Q_{eff} quantifies resolving power; networks with $G_{\text{az}} \lesssim 120$ recover full 3D structure.

(8) Proposed Community Standard SVP. The IQI framework separates high-reliability from saturated regimes across seven networks spanning $\approx 11\times$ in σ_h (GEOFON $\sigma_h = 7.5$ km to Hi-Net Noto $\sigma_h < 0.5$ km).

(9) Four Falsifiable Predictions and One Proposed Extension. P1–P4 carry explicit statistical tests at $\alpha = 0.05$. P5 introduces a topological-distance test as a proposed extension.

Editorial synthesis. The central methodological result is not the numerical value of a single dimension, but the demonstration that precision-conditioned inference can separate true structural signal from boundary-induced artifacts in a reproducible, transferable way across independent seismic networks.

Seven-Point Quality Checklist for Seismic Fractal Studies

1. Report σ_h and σ_v with stated uncertainty.
2. Verify $\sigma_h < \sigma_c = 2.3 \pm 0.4$ km or flag as potentially saturated.
3. Report both P_{boundary} and KL; never KL alone.
4. Run the Zaccagnino test; report S or declare inapplicability.
5. Calculate and report Q_{eff} including G_{az}.
6. Test at minimum four alternative prior families.
7. Evaluate against P1–P4.

Ethics and Conflict of Interest

The authors declare no financial or personal conflicts of interest.

Acknowledgments

We thank **NIED** for data access authorization (Sanction-2025@bosai.go.jp, December 2025) and the **ISC-GEM team** for institutional support and data workflow guidance (isc-gem@isc.ac.uk). Numerical analysis and visualization were performed using the **Python** scientific stack, including **NumPy**, **SciPy**, **Matplotlib**, and **Pandas**. We thank **Marc Martínez Sepúlveda**, **Hernando Rubén Chávez Fernández**, **Camila Paz Bravo**, and **Pablo Cingolani**, along with the entire team at **CEDESUR**. We also acknowledge **Ernesto Villanueva** and **Juan Pastor González** (UNAJ) for institutional support.

Data Availability Statement

USGS: https://earthquake.usgs.gov/earthquakes/. **Hi-Net (NIED):** restricted access via formal application and approval at https://hinetwww11.bosai.go.jp/auth/?LANG=en; for this study, access was granted for a limited period under NIED authorization. Public VRML hypocenter resources (2001–2005) are available at https://www.hinet.bosai.go.jp/topics/VRML/?LANG=en. **SCSN:** https://scedc.caltech.edu/. **GeoNet:** event portal used in this study: https://www.geonet.org.nz/earthquake. **Swiss-SED / EIDA:** https://www.orfeus-eu.org/data/eida/, 2000–2026, $M_c = 1.5$. **GEOFON:** https://geofon.gfz-potsdam.de/, 2007–2026, $M_c = 3.3$. **ISC-GEM:** V12.1 catalogue (DOI: 10.31905/D808B825) requires registration and institution-level request/approval; distribution is provided by ISC via request-specific delivery, not open bulk download. **Sysmic:** https://github.com/FacundoFirmenich/sysmic (GPL-3.0); Zenodo DOI: 10.5281/zenodo.18480821.

Sysmic Framework:

- **Primary repository:** https://github.com/FacundoFirmenich/sysmic (GPL-3.0 License).
- **Zenodo DOI:** 10.5281/zenodo.18480821.
- **Docker/Colab/Streamlit access:** all deployment and one-click execution resources are distributed within the same GitHub repository (documentation and launch instructions in `README.md`).
- **Pedagogical and multilingual resources:** `resources/multimedia/` includes didactic material in English, Spanish, and Portuguese.

The Sysmic framework is designed for open and reproducible science, combining multilingual accessibility, hardware-aware implementation, and transparent workflows.

Hardware Disclosure: This research was carried out on a mid-range 2016 laptop (Intel i5-6200U, 8–16 GB DDR3 RAM, SSD, 128 MB dedicated VRAM). Workflows remain feasible with 8 GB RAM, with longer runtimes. This shows that the full pipeline can be reproduced without high-end hardware.

Author Contributions

Facundo Firmenich, **Pau Firmenich**, and **León Firmenich** contributed to the formulation of the fundamental scientific question, framework conceptualization, and final approval of the manuscript and associated software release. **Facundo Firmenich** and **Pau Firmenich** contributed to methodological design, critical review and editing, and validation of the software architecture. **Pau Firmenich** and **León Firmenich** provided continuous supervision and overall project oversight. **Facundo Firmenich** was responsible for data curation, formal analysis, investigation, visualization, project administration, and original-draft writing.

AI-Assisted Development Disclosure

LLMs Claude, Gemini, DeepSeek, and Qwen were used for prototyping, coding, and translation, complemented by Wolfram Alpha (free tiers) for symbolic verification. All AI-generated content underwent exhaustive and indispensable human verification. No paid API subscriptions were used.

References

Aki, K. (1981). A probabilistic synthesis of precursory phenomena. In D. W. Simpson & P. G. Richards (Eds.), *Earthquake Prediction*, Maurice Ewing Ser., vol. 4, pp. 566–574. AGU.

Ben-Zion, Y. (2008). Collective behavior of earthquakes and faults. *Rev. Geophys.*, **46**, RG4006.

Cohen, J. (1988). *Statistical Power Analysis for the Behavioral Sciences* (2nd ed.). Lawrence Erlbaum.

Simoes, M., Daub, E. G., & Trugman, D. T. (2024). Global correlation dimension of seismicity. *Communications Earth & Environment*, **5**, 1–10. doi:10.1038/s43247-024-01306-0

Firmenich, F., Firmenich, P., & Firmenich, L. (2026). Sysmic v8.0.0: Precision-Calibrated Fractal Tomography Framework. *Zenodo*. doi:10.5281/zenodo.18480821.

Corral, Á., and González, Á. (2019). Power law size distributions in geoscience revisited. *Earth and Space Science*, **6**, 673–697.

Enescu, B., and Ito, K. (2005). Spatial analysis of the frequency-magnitude distribution and decay rate of aftershock activity of the 2000 Western Tottori earthquake. *Earth Planets Space*, **54**, 847–859.

Falconer, K. (2014). *Fractal Geometry* (3rd ed.). Wiley.

Firmenich, F., Firmenich, P., and Firmenich, L. (2025). Multi-Planar Hierarchy in Pan-American Seismic Fractality. *EarthArXiv*. doi:10.31223/x5rf3v

Foreman-Mackey, D., Hogg, D. W., Lang, D., and Goodman, J. (2013). emcee: The MCMC Hammer. *Publ. Astron. Soc. Pac.*, **125**, 306–312.

Gardner, J. K., and Knopoff, L. (1974). Is the sequence of earthquakes in Southern California Poissonian? *Bull. Seismol. Soc. Am.*, **64**, 1363–1367.

Grassberger, P., and Procaccia, I. (1983). Measuring the strangeness of strange attractors. *Physica D*, **9**, 189–208.

Green, H. W., and Houston, H. (1995). The mechanics of deep earthquakes. *Annu. Rev. Earth Planet. Sci.*, **23**, 169–213.

Hauksson, E., Yang, W., and Shearer, P. M. (2012). Waveform relocated earthquake catalog for southern California (1981–2011). *Bull. Seismol. Soc. Am.*, **102**, 2239–2244.

Hedges, L. V., and Olkin, I. (1985). *Statistical Methods for Meta-Analysis*. Academic Press.

Hirth, G., and Kohlstedt, D. L. (2003). Rheology of the upper mantle and the mantle wedge. *Geophys. Monogr.*, **138**, 83–105.

International Seismological Centre (2025). *ISC-GEM Global Instrumental Earthquake Catalogue V12.1*. doi:10.31905/D808B825

Kagan, Y. Y. (2007). Earthquake spatial distribution: the correlation dimension. *Geophys. J. Int.*, **168**, 1175–1194.

Kagan, Y. Y., and Jackson, D. D. (2000). Probabilistic forecasting of earthquakes. *Geophys. J. Int.*, **143**, 438–453.

Kagan, Y. Y., and Knopoff, L. (1980). Spatial distribution of earthquakes. *Geophys. J. R. Astr. Soc.*, **62**, 303–320.

Kantelhardt, J. W., et al. (2002). Multifractal detrended fluctuation analysis. *Physica A*, **316**, 87–114.

Kato, A., Fukuda, J., and Nakagawa, S. (2023). Deep learning-assisted earthquake catalog for the 2023 Noto Peninsula earthquake sequence. *Earth, Planets and Space*, **75**(1), 1–15.

Killick, R., Fearnhead, P., & Eckley, I. A. (2012). Optimal detection of changepoints. *J. Am. Stat. Assoc.*, **107**, 1590–1598.

King, G. C. P., Stein, R. S., & Lin, J. (1994). Static stress changes and the triggering of earthquakes. *Bull. Seismol. Soc. Am.*, **84**, 935–953.

Lahiri, S. N. (2003). *Resampling Methods for Dependent Data*. Springer.

Marstrand, J. M. (1954). Some fundamental geometrical properties of plane sets of fractional dimensions. *Proc. Lond. Math. Soc.*, **4**, 257–302.

Mondal, S., Bhattacharyya, D., & Chatterjee, S. (2019). Multifractal analysis of earthquake catalogs. *Pure Appl. Geophys.*, **176**, 2855–2872.

Nakagawa, S., & Schielzeth, H. (2013). A general and simple method for obtaining R^2 from GLMMs. *Methods Ecol Evol*, **4**, 133–142.

Nanjo, K., Nagahama, H., & Satomura, M. (2005). Fractal properties of spatial distributions of aftershocks. *Tectonophysics*, **233**, 209–220.

NIED (2019). *Hi-net* [Data set]. doi:10.17598/NIED.0003

Obara, K., et al. (2005). A densely distributed high-sensitivity seismograph network in Japan: Hi-net. *Rev. Sci. Instrum.*, **76**, 021301.

Ogata, Y. (1988). Statistical models for earthquake occurrences. *J. Am. Stat. Assoc.*, **83**, 9–27.

Peacock, S. M. (2001). Are the lower planes of double seismic zones caused by serpentine dehydration? *Geology*, **29**, 299–302.

Ripley, B. D. (1977). Modelling spatial patterns. *J. R. Stat. Soc. B*, **39**, 172–212.

Scholz, C. H. (2019). *The Mechanics of Earthquakes and Faulting* (3rd ed.). Cambridge.

Stein, R. S. (1999). The role of stress transfer in earthquake occurrence. *Nature*, **402**, 605–609.

Stoyan, D., Kendall, W. S., & Mecke, J. (1995). *Stochastic Geometry and Its Applications* (2nd ed.). Wiley.

Theil, H. (1950). A rank-invariant method of linear and polynomial regression. *Indag. Math.*, **12**, 85–91.

Theiler, J. (1990). Estimating fractal dimension. *J. Opt. Soc. Am. A*, **7**(6), 1055–1073.

Tosi, P., Vinciguerra, S., & De Rubeis, V. (1998). Multifractal analysis of spatial distribution of microearthquakes in the Kanto region. *Phys. Earth Planet. Inter.*, **109**(3-4), 243–256.

Traag, V. A., Waltman, L., and van Eck, N. J. (2019). From Louvain to Leiden. *Sci. Rep.*, **9**, 5233.

Turcotte, D. L. (1997). *Fractals and Chaos in Geology and Geophysics* (2nd ed.). Cambridge.

Vincenty, T. (1975). Direct and inverse solutions of geodesics on the ellipsoid. *Surv. Rev.*, **23**, 88–93.

Zaccagnino, D., Doglioni, C., & Telesca, A. (2022). Correlation between seismicity and fractal dimension of fault systems. *Pure Appl. Geophys.*, **179**, 2543–2560.

Zaccagnino, D., et al. (2024). Scale-invariant properties of seismicity. *Commun. Earth Environ.*, **5**, 1–10.

A Proof of Theorem 1

Let $\theta \in [\theta_{\min}, \theta_{\max}]$, $p(\theta_{\max}) > 0$, $\epsilon = \mathcal{I}_{\text{lik}}/\mathcal{I}_{\text{prior}}$. Expanding $\log L$ around $\hat{\theta}$: $\log L \approx \log L(\hat{\theta}) - \frac{1}{2}\mathcal{I}_{\text{lik}}(\theta - \hat{\theta})^2$. As $\epsilon \to 0$: $\mathcal{I}_{\text{lik}} \to 0$, so $\exp[-\frac{1}{2}\mathcal{I}_{\text{lik}}(\theta - \hat{\theta})^2] \to 1$ uniformly, and $p(\theta|\mathbf{d}) \to p(\theta)$. Since $p(\theta_{\max}) > 0$: $P_{\text{boundary}} \to \int_{\theta_{\max}-\delta}^{\theta_{\max}} p(\theta)\, d\theta > 0$.

B Derivation of σ_c (Eq. 6)

From Eq. (5) with $\eta(\sigma_c) = \exp(-\sigma_c/\lambda)$:

$$-\frac{2\sigma_c}{\lambda} = \log\left(\frac{k^* \mathcal{I}_{\text{prior}} \sigma_{D_2}^2 N_{\text{pairs}}}{Q_{\text{eff}}\, N_{\text{eff}}}\right), \quad \sigma_c = -\frac{\lambda}{2}\log(\cdots).$$

With Japan/Noto parameters ($\lambda = 5.0$ km, $k^* = 2.80$, $\mathcal{I}_{\text{prior}} = 0.444$, $\sigma_{D_2} = 0.048$, $Q_{\text{eff}} = 0.32$, $N_{\text{eff}}/N_{\text{pairs}} = 1/40$): $\sigma_c = 2.31$ km.

C Deck-of-Cards Derivation and Continuum Limit Verification

C.1 Continuum Limit and Geometric Constant $Q = 2/3$

$$\frac{n}{\delta}\int_0^r c_0\,\pi(r^2 - h^2)\,dh = \frac{n\,c_0\,\pi}{\delta}\left[r^2 h - \frac{h^3}{3}\right]_0^r = \frac{2}{3}\,\frac{n\,c_0\,\pi r^3}{\delta}. \tag{20}$$

C.2 Numerical Verification

Table 17: Continuum limit verification ($\delta = 5$ km, $n = 20$ planes).

r (km)	r/δ	$n/(r/\delta)$	D_3^{cont}	D_3^{disc}	$\lvert\Delta D_3\rvert$
0.5	0.10	200.0	2.063	2.063	0.000
2.0	0.40	50.0	2.211	2.211	0.000
5.0	1.00	20.0	2.400	2.381	0.019
10.0	2.00	10.0	2.571	2.551	0.020
15.0	3.00	6.7	2.667	2.645	0.022
25.0	5.00	4.0	2.769	2.740	0.029
50.0	10.00	2.0	2.870	2.820	**0.050**

Combined prediction uncertainty: $D_3^{\text{pred}} = 2.82 \pm 0.05\,(\text{syst.}) \pm 0.05\,(1\sigma\ \text{bootstrap})$, combined ± 0.07.

D Monte Carlo Calibration of k^*

Grid: $D_3 \in \{1.5, ..., 3.0\}$ (9 levels) $\times$ $\sigma \in \{0.05, ..., 15\}$ km (11 levels); 50 replicas per cell; $N = 5{,}000$ events; total 4,950 catalogs. Result: $k^* = 2.80 \pm 0.30$ (95% CI); $\lambda = 5.2 \pm 0.8$ km; $R^2 = 0.94$.

E Calibration of Q_{eff} Weights

Weights calibrated before any D_3 inference via weighted least squares against $\rho_{M<2.0}$ ($R^2 = 0.89$) and Δ_{RMS} ($R^2 = 0.82$). Post-hoc: $r(Q_{\text{eff}}, P_{\text{boundary}}) = -0.83$ ($p = 0.008$).

For transparency, uncertainty propagation to Q_{eff} and σ_c^{eff} follows Eq. (18). This keeps classification uncertainty explicit when comparing catalogs close to the barrier.

F Proof of Proposition 1

Let $\mathcal{P}_2 = (1-\varepsilon)\mathcal{N}(2.82, 0.05^2) + \varepsilon\,\delta_{3.0}$. For $\varepsilon < 0.1$: $|\text{KL}[\mathcal{P}_1\|\pi] - \text{KL}[\mathcal{P}_2\|\pi]| < 0.52$ nats, yet $P_{\text{boundary}}(\mathcal{P}_2) = 100\varepsilon\%$.

G Operational Justification of $\mathcal{I}_{\text{prior}} = 0.444$

For Uniform$(1.5, 3.0)$, canonical Fisher information is zero. We adopt the operational definition $\mathcal{I}_{\text{prior}} = 1/(b-a)^2 = 1/(1.5)^2 = 0.444$, representing inverse squared support width. This is not a Fisher information in the classical sense but an operational regularization constant chosen so that Eq. (5) reproduces the Monte Carlo transition at $\sigma_c \approx 2.3$ km. Robustness: σ_c varies <0.6 km across all four prior families. Theorem 1 guarantees the qualitative saturation result independent of this definition.

H VRML 3-D Analysis and Scale Calibration

Source: `hinet_hypo.2001-2005.M1.5.wrl` ($N = 192{,}387$). Scale: 1 unit $= 196 \pm 4$ km (Monte Carlo, 100 trials). Result: model-independent adaptive-window D_2 estimate (reported in Fig. 17 annotation). Independent of Bayesian MCMC.

I Model Comparison for Depth-Dependent Planarization

Table 18: Model comparison statistics.

Model	#par	$\ln \hat{\mathcal{L}}$	AIC	AICc	BIC	RMSE
Linear	2	1.53	−0.94	9.0	2.3	0.154
Exponential	4	6.93	−5.86	5.7	−1.8	0.017

ΔAICc = 3.3; ΔBIC = 4.1.

J Synthetic Geometry Validation (Test 0)

This appendix provides the In-Sample Consistency benchmark (Test 0, Section 2.5).

Table 19: Algorithm accuracy on known geometries (Test 0).

Geometry	Theoretical D_2	Measured D_2	Error
2D Plane (embedded 3D)	2.00	2.01 ± 0.01	0.5%
3D Cube	3.00	2.98 ± 0.02	0.7%
Sierpiński Carpet	1.89	1.91 ± 0.03	1.1%
Multi-planar deck	$H > 0$ (qual.)	$H > 0$ in 95% trials	—

Maximum error: **1.1%**. All synthetic geometries yield $P_{\text{boundary}} < 1\%$ when the true dimension is sub-volumetric, confirming that saturation flags are attributable to information loss, not algorithmic bias.

K Methodological Sensitivity Analysis

Table 20: Cross-dimensional sensitivity: core metrics invariance.

Metric	Baseline	Min	Max	CV (%)
D_2 (Mean)	2.234	2.218	2.251	0.7
$H > 0$ Recovery	66.7%	66.7%	83.3%	12.3
D_3 Convergence	3.00	2.97	3.03	1.0
$D_{\text{graph}} < D_2$	100%	100%	100%	0

Variations tested: three M_c strategies (Global MAXC, Regional MAXC, Fixed $M_c = 3.5$); three scaling-region algorithms (Uniform$[1.5, 3.0]$ prior [current approach], Adaptive R-max, Fixed Window); three coordinate systems (Local Metric, ECEF, Normalized Unit Cube). Core findings persist across all variations (CV $< 2\%$ for quantitative metrics).

Supporting Information S1: ISC-GEM $M \geq 8$ Global Analysis (Exploratory)

Contents of Supporting Information:

1. Text S1: ISC-GEM $M \geq 8$ Global Analysis (Exploratory)
2. Table S1: ISC-GEM $M \geq 8$ exploratory summary.

This supporting information provides the extended exploratory results from the complete analysis of the ISC-GEM Global Instrumental Earthquake Catalogue (Version 12.1), specifically focusing on $M \geq 8$ megathrust and mega-rupture events from 1964 to 2019. Consistent with the main text, these global data exhibit coarse horizontal precision ($\sigma_h \approx$ 10–30 km), leading to firm saturation when processed via the SVP protocol.

Text S1: ISC-GEM $M \geq 8$ Global Analysis (Exploratory)

Of 430 event-window combinations, only 26 (6.0%) met the $N \geq 100$ Grassberger–Procaccia quality requirement. Mean $D_2 = 0.94 \pm 0.23$ for valid post-event windows, consistent with aftershock concentration on planar rupture surfaces but insufficient for quantitative tectonic inference.

Table 21: ISC-GEM $M \geq 8$ exploratory summary (Table S1).

Metric	Value	Note
Total event-windows	430	PRE / MAIN / POST
Valid D_2 estimates	26 (6.0%)	$N \geq 100$ threshold
Mean D_2 (valid)	0.94 ± 0.23	Planar aftershock distributions
Dominant valid type	POST (14/26)	Aftershock densification
$\sigma_h < 2.3$ km events	4	All $P_{\text{boundary}} < 3\%$
$\sigma_h > 3$ km events	22	17/22 have $P_{\text{boundary}} > 5\%$; 12/22 have $P_{\text{boundary}} > 90\%$ (fully saturated)

No conclusions about specific source regions should be drawn from these sparse data. For full cross-validation and rigorous application of the Sysmic Framework's SVP algorithm on higher-yield catalogs, refer to Section 4 of the main text.